Quaternary International 310 (2013) 124–139

Contents lists available at SciVerse ScienceDirect

Quaternary International

journal homepage: www.elsevier.com/locate/quaint

Influence of the Pacific Decadal Oscillation, El Niño-Southern Oscillation and solar forcing on climate and primary productivity changes in the northeast Pacific

R. Timothy Patterson [a,*], Alice S. Chang [a,1], Andreas Prokoph [a], Helen M. Roe [b], Graeme T. Swindles [c]

[a] Department of Earth Sciences and Ottawa-Carleton Geoscience Center, Carleton University, 1125 Colonel By Drive, Ottawa, Ontario K1S 5B6, Canada
[b] School of Geography, Archeology and Palaeoecology, Queen's University Belfast BT7 1NN, Northern Ireland, United Kingdom
[c] School of Geography, University of Leeds, Leeds LS2 9JT, United Kingdom

ARTICLE INFO

Article history:
Available online 9 February 2013

ABSTRACT

Evidence of 11-year Schwabe solar sunspot cycles, El Niño-Southern Oscillation (ENSO) and the Pacific Decadal Oscillation (PDO) were detected in an annual record of diatomaceous laminated sediments from anoxic Effingham Inlet, Vancouver Island, British Columbia. Radiometric dating and counting of annual varves dates the sediments from AD 1947–1993. Intact sediment slabs were X-rayed for sediment structure (lamina thickness and composition based on gray-scale), and subsamples were examined for diatom abundances and for grain size. Wavelet analysis reveals the presence of ~2–3, ~4.5, ~7 and ~9–12-year cycles in the diatom record and an ~11–13 year record in the sedimentary varve thickness record. These cycle lengths suggest that both ENSO and the sunspot cycle had an influence on primary productivity and sedimentation patterns. Sediment grain size could not be correlated to the sunspot cycle although a peak in the grain size data centered around the mid-1970s may be related to the 1976–1977 Pacific climate shift, which occurred when the PDO index shifted from negative (cool conditions) to positive (warm conditions). Additional evidence of the PDO regime shift is found in wavelet and cross-wavelet results for *Skeletonema costatum*, a weakly silicified variant of *S. costatum*, annual precipitation and April to June precipitation. Higher spring (April/May) values of the North Pacific High pressure index during sunspot minima suggest that during this time, increased cloud cover and concomitant suppression of the Aleutian Low (AL) pressure system led to strengthened coastal upwelling and enhanced diatom production earlier in the year. These results suggest that the 11-year solar cycle, amplified by cloud cover and upwelling changes, as well as ENSO, exert significant influence on marine primary productivity in the northeast Pacific. The expression of these cyclic phenomena in the sedimentary record were in turn modulated by the phase of PDO, as indicated by the change in period of ENSO and suppression of the solar signal in the record after the 1976–1977 regime shift.

1. Introduction

At the seasonal level, climate in southwestern British Columbia, is strongly influenced by changes in the relative strength and positions of the North Pacific High (NPH) and Aleutian Low (AL) atmospheric pressure systems. This results in predominantly upwelling conditions prevailing during the spring through to fall and downwelling conditions during the winter months (Ware and Thomson, 2000). At subdecadal and decadal time scales the climate is further modified by El Niño-Southern Oscillation (ENSO) and the Pacific Decadal Oscillation (PDO) (Shabbar et al., 1997; Mantua and Hare, 2002). These various climate cycles do not act independently of each other, with the impact of one or more influences superimposed on one another (Goodrich, 2007). The full nature of these interactions is still not completely understood and is the subject of ongoing research.

* Corresponding author.
E-mail address: tpatters@earthsci.carleton.ca (R. Timothy Patterson).
[1] Current address: Department of Forest and Conservation Sciences, University of British Columbia, Vancouver, BC V6T 1Z4, Canada.

1040-6182/$ – see front matter © 2013 Elsevier Ltd and INQUA. All rights reserved.
http://dx.doi.org/10.1016/j.quaint.2013.02.001

Effingham Inlet provides a unique environment to assess the relationship between the various climatic influences in the region due to there being a direct response of the resident waters within Effingham Inlet to the adjacent open waters of the eastern North Pacific (Thomson, 1981). The anoxic and dysoxic conditions that prevail at depth within Effingham Inlet thus provide ideal conditions for the excellent preservation of annually deposited laminated sediments and diatom remains which archive a continuous record of seasonal-scale climate change spanning much of the Holocene (Patterson et al., 2000; Chang et al., 2003). Previous research on Holocene cores from Effingham Inlet has resulted in recognition of various climatic cycles and trends, including ENSO, PDO and solar cycles, based on comparisons with modern analogs from other locations, that have influenced sedimentological and biological deposition in the inlet (e.g. Chang et al., 2003; Patterson et al., 2004, 2005, 2011; Ivanochko et al., 2008). However, as the instrumental record in the region only extends back to the early 20th century, it was impossible to correlate these Holocene proxy records with known meteorological and oceanographic events.

This paper details an analysis of diatom floras (Class Bacillariophyceae) and sedimentology of a freeze core collected from Effingham Inlet. This record, composed of continuously deposited annually laminated sediments dating from AD1947–1993, is analyzed for evidence of climatic drivers that impact the region (e.g. ENSO, PDO and solar cycle influence). Based on comparisons with historical meteorological time series data and on a review of ocean–atmosphere processes we propose potential mechanisms to explain the connection between these climatic drivers and the observed primary productivity and sedimentation patterns.

2. Northeast Pacific climate and oceanography

Climate and oceanography in the northeast Pacific is governed by the positions of the AL pressure system from October to March, and the NPH pressure system from April to September (Fig. 1), which are in turn modulated by the jet stream and ENSO cycles. Less well understood are regionally modified, decadal (e.g., PDO) to centennial-scale cycles, which seem to arise from global scale teleconnections that are superimposed on these phenomena (Ware and Thomson, 2000; Patterson et al., 2004; Ivanochko et al., 2008). Modern coastal southwestern Vancouver Island has a cool-temperate climate where precipitation can reach up to 400 cm annually (Natural Resources Canada, 2009). During the cool, rainy winters, the coastal region is affected by frontal systems associated with cyclonic storms. During the relatively warmer and drier summers, the coastal region is influenced by large anticyclonic systems.

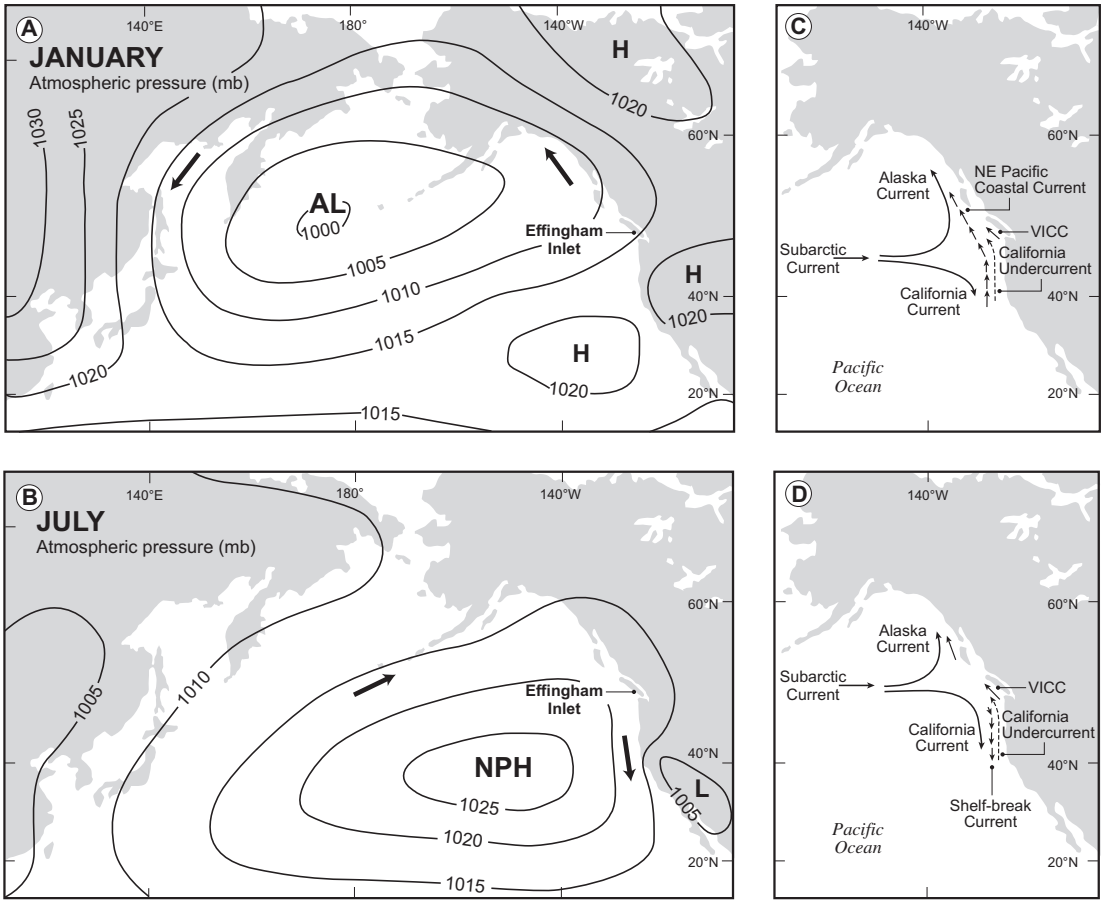

Fig. 1. Regional oceanography. Main ocean–atmosphere circulation features and surface currents for the NE Pacific region in winter (A,C) and summer (B,D) months. In the summer, northerly North Pacific High (NPH) winds generate the southward Shelf-Break Current at the surface. During the winter, southerly Aleutian Low (AL) winds generate a northward drift producing the NE Pacific Coastal Current. The Vancouver Island Coastal Current (VICC) and California Undercurrent are permanent features although they vary in strength seasonally (after Patterson et al., 2011).

The locations of the AL and NPH are important for determining the timing and intensity of seasonal upwelling and diatom blooms along the west coast of North America. Wind-induced annual upwelling along the west coast of Vancouver Island is prevalent from May through August when the NPH is situated at 38°N (Hickey, 1998). The upwelling is initiated in response to a seaward, wind-forced Ekman transport in the surface layer and coincides with the southeastward-flowing shelf-break current (Fig. 1). This spring/summer flow structure is driven by anticyclonic winds associated with the NPH pressure system (Thomson and Gower, 1998). The upwelling extends seaward of the 200-m shelf-break, with subsequent transport of deeper (>150 m) oxygenated and nutrient-rich slope waters onto the continental shelf, where it is carried landward through a series of submarine canyons (Thomson et al., 1989; Thomson and Ware, 1996; Ware and Thomson, 2005). The California Undercurrent, which flows north along the continental margin at a depth of about 300 m, also contributes poorly oxygenated and nutrient-rich water to the southwestern coast of Vancouver Island (Fig. 1). Estuarine inflow through Juan de Fuca Canyon transports the nutrient-rich water originating from both wind-induced upwelling and undercurrent advection into Juan de Fuca Strait (Fig. 2). These nutrient-rich waters undergo strong vertical mixing within the strait before eventually becoming entrained in a nutrient-rich surface outflow toward the open ocean (Crawford and Dewey, 1989). This nutrient-rich water mixes with upwelled continental shelf water and the California Undercurrent, then flows northward over the inner shelf as a component of the Vancouver Island Coastal Current where it can lead to a marked increase in phytoplankton production in the adjoining coastal inlets. During the autumn and winter, when the NPH shifts southward to 28°N, downwelling prevails as surface waters are deflected onshore from southeasterly winds associated with the AL.

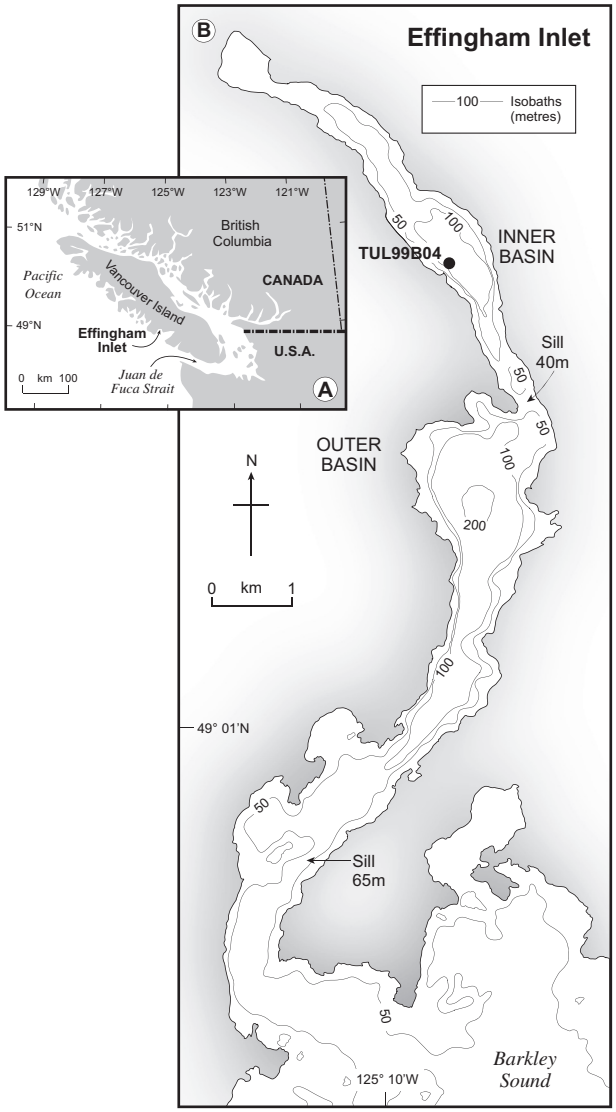

Fig. 2. Study area. (A) Location map of southern British Columbia showing geographic features discussed in this paper and location of Effingham Inlet on southwestern coast of Vancouver Island. (B) Details of Effingham Inlet showing location of freeze core TUL99B04 (after Patterson et al., 2011).

There is an observed correlation between the 11-year solar cycle and the locations of atmospheric pressure gyres (centers of action, COAs) over the North Pacific Ocean (Christoforou and Hameed, 1997; Hameed and Lee, 2005). During sunspot maxima, the AL pressure system moves west by as much as 700 km with respect to the COA during a sunspot minimum, while the NPH pressure system moves north by as much as 300 km with respect to the COA during a sunspot minimum (Christoforou and Hameed, 1997). During strong El Niño events, diatoms in the northeast Pacific tend to be displaced by southerly zooplankton and nanoplankton species due to the poleward propagation of warmer SSTs and simultaneously reduced coastal upwelling and nutrient delivery to the shelf regions. Such a population shift was witnessed off the British Columbia coast during the well-documented and strongest-recorded 1997–1998 El Niño (Mackas and Galbraith, 2002; Mackas et al., 2004; Harris et al., 2009). When conditions reversed in mid-1998, with the start of the strong La Niña event, southerly plankton receded and diatoms were re-established when upwelling resumed and surface nutrients increased (Zamon and Welch, 2005; Harris et al., 2009). The relative influence of ENSO events is closely linked to PDO. For example, when PDO and ENSO are in phase (positive PDO – El Niño or negative PDO – La Niña) ENSO winter climate signals in western North America are stronger and more stable. When PDO and ENSO are out of phase there is a weaker climate signal (Gershunov and Barnett, 1998; Goodrich, 2007). There is also evidence that the timing and intensity of PDO is influenced by the Gleissberg solar cycle (Shen et al., 2006), an 88-year amplitude modulation of the 11-year cycle. Less well studied are higher frequency solar influenced climate changes, which affect the track of the jet stream and in turn the relative seasonal positioning of the NPH and AL (Christoforou and Hameed, 1997).

3. Effingham inlet hydrology

Effingham Inlet opens to the Pacific Ocean via Barkley Sound (Fig. 2). The shoreline is steep and rocky except for low-lying marshy areas. The fjord measures 17 km in length, has an average width of 1 km, and contains two bedrock sills and two basins. Like most fjords on Vancouver Island, Effingham Inlet is classified as a low-runoff fjord (Pickard, 1963). Salinity, temperature, oxygen, density and other water property data indicate that Effingham Inlet experiences well-developed estuarine-type stratification throughout the year, with a year-round layer of fresh water at the surface (Patterson et al., 2000). In contrast to most coastal British Columbia inlets, peak discharge in Effingham Inlet occurs during the winter months as temperatures tend to stay above freezing and precipitation is at a maximum (Stronach et al., 1993). Peak runoff corresponds with more intense stratification. The low salinity surface layer becomes thinner and the

water column less stratified during the spring and summer as runoff diminishes and surface mixing is able to penetrate deeper into the water column (Chang et al., 2013; P. Whitfield, Environment Canada, unpublished data, 2010). The restricted nature of the fjord, the estuarine stratification, and high primary productivity lead to anoxia of the bottom waters within the inner basin, which excludes bioturbating macrobenthos and allows for the preservation of finely laminated sediments consisting mainly of clay and silt size components. A brown-colored, detritus-rich lamina, deposited during the autumn and winter, and an olive-colored, diatom-rich lamina, deposited during the spring and summer, comprise an annual varve (Chang et al., 2003; Chang and Patterson, 2005; Patterson et al., 2011). The bottom waters of the inner basin are periodically aerated by oxygenated waters entering from outside the inlet, but such occurrences are rare (Chang et al., 2013; Dallimore et al., 2005).

4. Materials and methods

4.1. Core handling

Freeze core TUL99B04 (49° 04.218′ N, 125° 09.429′ W; 123 cm long; 120 m water depth) was recovered from the uppermost part of the sediment column in the inner basin of Effingham Inlet in October 1999 (Fig. 2). The custom-made freeze corer (designed by J. Crusius, USGS Woods Hole, USA, based on existing designs, e.g., Hughen et al., 1996) consisted of a 10 cm^2 by 3-m long aluminum box insulated with syntactic foam on three sides. The one exposed side formed a flat, frozen surface on which the sediments could adhere. The bottom end of the box was tapered to ease penetration into the sediments, and the top of the box was fitted with a cryogenic temperature check valve from which CO_2 from dry ice could escape. Lead weights were loaded into the bottom end of the box, and the box was filled with a slurry of dry ice and alcohol. The corer was lowered into the sediments as perpendicularly as possible, and remained in the sediments for 30 min, which permitted an approximately 3-cm thick rind of sediment to adhere to the corer. Upon recovery, the frozen sediment was carefully removed from the corer, wrapped in protective layers, and stored in a freezer until ready for processing.

Using a bandsaw, the frozen core was slabbed perpendicular to the bedding plane to a thickness of 1–1.5 cm and 15-cm lengths, and the slabs X-rayed to elucidate internal sedimentary structures not visible on the core surface. The slabs were X-rayed with a Faxitron Series 43805-N X-ray system and Agfa™ D7 film while still frozen. The film negatives were scanned by a computer and converted into positive gray-scale images with photograph editing software. The positive images revealed that the normally horizontal sedimentary fabric was at an angle due to shearing during the coring process (see Fig. 3D). The most severely sheared sediments occurred in a 0.5-cm thick zone near the freeze corer surface. Measurements of varve thickness were made on the positive images on the least-sheared portion of the core, and the sheared zone was removed from the slabs prior to subsampling.

4.2. Analysis of annually deposited varves

The upper 32 cm of the freeze core is laminated while the rest of the core consists of a slump deposit. Chang et al. (2003) confirmed the annual nature of the laminae (varves) deposited in Effingham Inlet. The chronology of the laminated section was determined by counting varves and dating the sediments with ^{137}Cs and ^{210}Pb. From the X-radiograph, 46 varves were quantified from the top of the slump deposit to the top of the core (Fig. 3). The basal age of the laminated section is constrained because the slump deposit has been determined to represent deposition from an $M = 7.6$ earthquake that occurred on 23 June 1946 in central Vancouver Island (Rogers, 1980). This slump deposit is found in correlative freeze cores throughout Effingham Inlet (Dallimore et al., 2005; Hay et al., 2009) and in nearby Saanich Inlet in southeastern Vancouver Island (Blais-Stevens et al., 1997; Blais-Stevens and Patterson, 1998). Thus, the oldest varve was assigned a calendar year of 1947. A total of 29 samples for radiometric dating were taken at successive 1 cm intervals beginning at a core depth of 3 cm where there was enough material to be dated. A minimum of 10 g (wet, 1 g dry) of sediment was obtained for both the ^{137}Cs analysis and ^{210}Pb analyses (the latter analysis requires only 5 g of wet sediment or 0.5 g dry). Only one sample from each horizon was required because non-destructive ^{137}Cs analysis was performed before destructive ^{210}Pb analysis. The samples were dried in an oven for 7 h at 70 °C until fully desiccated and then ground to a powder. The radiometric analysis was performed by GEOTOP Laboratories (University of Québec at Montreal).

Using the X-radiographs as a guide, varves were sliced from the frozen core with a blade parallel to bedding planes, producing two sets of 42 subsamples for quantitative diatom and grain size analyses (Fig. 3). For diatom analysis, the samples were freeze-dried and processed by transferring ~40 mg of dry sediment into 20-mL glass scintillation vials. Chemical treatments of the sediments and preparation of the microscope slides followed methods described in Chang and Patterson (2005). Diatom counting rules followed that of Schrader and Gersonde (1978), using an Olympus BX-51 light microscope equipped with a differential interference contrast filter, at 1000× magnification. At least 500 diatom valves were counted per sample, using at least 40 random fields of view, except for three samples (B04-27, 35 and 36) where diatoms were more abundant and fewer fields of view were used. Taxa were identified to the species level where possible (Fig. 4). Two main types of *Skeletonema costatum* were identified, including a larger, robust and more abundant form, as well as a smaller, weakly silicified, and less abundant form. Such morphological designations for *S. costatum* have been used in previous studies in coastal British Columbia (Sancetta and Calvert, 1988; Hobson and McQuoid, 2001; Hay et al., 2003), although recent reclassification suggests that the slightly different *Skeletonema* morphotypes represent a suite of ecologically similar but genetically separate species (cf. Sarno et al., 2005; Zingone et al., 2005), which we do not distinguish here. *Chaetoceros* spp. resting spores (CRSs) and rare but poorly preserved *Chaetoceros* spp. vegetative cells were counted as one group separately from the other diatom species. *Chaetoceros* spp. abundances can be overwhelming, and separating this group from the rest of the diatom taxa can highlight trends in the less abundant species (cf. Hemphill-Haley and Fourtanier, 1995). The absolute abundance of diatoms and CRS (number of valves per gram of dry sediment) and species relative abundance (%) were calculated using the equations of Chang and Patterson (2005). Spores of other diatom species (e.g., *Stephanopyxis*, *Thalassiosira*, etc.) were not enumerated. Although CRS data are shown for comparison, we do not include them or other spores in the statistical analyses, and only involve vegetative (reproductive) cells as representatives of primary productivity.

For grain size analysis, 25 mL of deionized water was added to 0.5 g of freeze-dried sediment. The sediment samples were digested in 30% H_2O_2 to remove organic matter centrifuged and the supernatant decanted. The resulting sediment paste was mixed with a spatula to homogeneity and then subsampled for grain size

Table 1
Linear correlation between sunspot number, climate, diatom and sedimentary data.

	1	2	3	4	5	6	7	8	9
1. Sunspot number									
2. ALI	−0.12								
3. NPI (spring)	−0.32[a]	−0.04							
4. NPI	−0.04	−0.61[b]	0.50[b]						
5. SST	0.15	0.69[b]	−0.12	−0.54[b]					
6. SST (spring)	0.06	0.27	0.24	−0.14	0.41[a]				
7. Precipitation	−0.30[a]	0.17	0.25	−0.06	0.05	0.14			
8. Grain size	−0.12	0.07	0.20	−0.04	−0.06	0.28[a]	−0.01		
9. Diatom abundance	−0.26	−0.15	0.20	0.27	−0.14	−0.23	0.05	0.19	
10. Varve thickness	−0.48[b]	0.02	0.28[a]	0.15	0.01	−0.10	0.07	0.29[a]	0.43[a]

Cross 1 year	Sunspot number	ALI	NPI (spring)	NPI	SST	SST (spring)	Precipitation
Grain size	−0.09	0.12	0.09	0.06	0.32[a]	−0.03	0.21
Diatom abundance	−0.42[b]	−0.14	0.14	0.23	−0.04	−0.02	0.12
Varve thickness	−0.48[b]	0.01	0.20	0.15	−0.01	0.06	0.13

Note: see text for explanations of abbreviations ALI, NPI and SST.
[a] 90% confidence.
[b] 95% confidence.

analysis. The subsamples were then mixed with a 1% sodium hexametaphosphate solution and ultrasonically disaggregated for 3 min to deflocculate clay particles. The sediment slurry was poured into a Galai CIS-1 laser granulometer and the grain size distribution determined from a combination of biogenic (siliceous diatoms) and abiogenic (detrital) particles (Table 1). Diatom concentrations and sediment weights used for grain size analysis were not corrected for salt content.

4.3. Cyclostratigraphy and wavelet analysis

Wavelet analysis can be used as a cyclostratigraphic method for detecting cycles in time series data by transforming information from the depth- or time-domain into the spectral domain using short filtering functions called "wavelets" (see Prokoph and Patterson, 2004a). Wavelet analysis was initially used as a filtering and data compression method in the 1980s (e.g., Morlet et al., 1982) and has since been widely applied in geophysics and other areas of earth sciences (e.g., Grossman and Morlet, 1984; Patterson and Fowler, 1996; Prokoph et al., 2000; Prokoph and Patterson, 2004b). Because sediment accumulation naturally varies through time, time series data from a sedimentary core inherently contains information on a uniform depth scale but on a non-uniform time scale. If the sedimentation rate is known for the core, or the time interval for the deposition of individual beds is known (in this case, varves are annual), then cycles can be defined providing that sedimentation is truly being influenced by external (allocyclic) forces, such as the changing of seasons. In such cases wavelet analysis can convert the data into an equidistant time scale, and extract two records in time-domain: sedimentation rate (e.g., varve thickness; Appendix 1); and sedimentary composition (e.g., sediment color; Appendix 2) (Prokoph and Patterson, 2004a). Subsequently another wavelet analysis on the two time-domain-records can detect cyclical and quasi-cyclical oceanographic and climate oscillations, as well as gradual and abrupt sedimentary changes. Traditional spectral analysis may be able to display the variance (or "power") according to frequencies (or cycle lengths) assuming stationarity of the signals, but all time information is lost (e.g., Davis, 1986). Wavelet analysis and the resulting scalogram have the benefit of visually displaying the position of cycles through time along the length of the core, and give an idea of how shorter-length cycles are embedded within longer cycles through time (e.g., Patterson et al., 2004, 2005, 2007). However, spectral analysis using a Discrete Fourier transform is able to provide estimates of the "power" (signal variance per unit frequency band) and better statistically defined confidence levels of the cycle as a function of frequency (Davis, 1986). Continuous wavelet transform and spectral analyses were performed on the records of X-radiograph gray-scale data, grain size, and absolute diatom abundance in both depth and time domains. Wavelet analysis was also performed on both robust and weakly silicified variants of *S. costatum*, as these were found to be dominant taxa, as well as total annual precipitation and April to June precipitation. The April to June precipitation data subset was chosen for the cross-wavelet analysis as this corresponds to *S. costatum* peak production in the region (McQuoid and Hobson, 1997). These data are shown separately to highlight population trends through time.

Gray-scale values, sedimentation rates and cycle periodicities were determined from a digital line scan of 256 shades of gray on the X-ray positive images of the laminated interval. The image resolution of 1 pixel is equal to 0.025 mm. Background gray-scale variability of the X-ray images was color corrected and standardized using the image processing software IMAGEJ so that color information could be statistically analyzed (Prokoph and Patterson, 2004b). Line scans 3 pixels wide (0.3 mm) were taken perpendicular to sedimentary laminae and the gray-scale values averaged. The gray-scale values were saved as ASCII files (pixel number, gray-scale value). Further editing of the line scans involved correcting depth values from pixel numbers, replacement of extreme gray-scale values (e.g. due to small cracks, etc.) by using adjacent gray-scale values (after Schaaf and Thurow, 1994). Time series analysis was carried out using the computer program CWTX.F (after Prokoph and Barthelmes, 1996).

Time series analysis of *S. costatum*, the weakly silicified variants of *S. costatum*, as well as total annual precipitation and April to June precipitation, were carried out using PAST software (Hammer et al., 2001). Spectral analysis (A Lomb-Scargle Fourier transform method 'REDFIT') was used to statistically test a null hypothesis of red (autocorrelated) noise in the data (Schulz and Stattegger, 1997; Schulz and Mudelsee, 2002) because red-noise backgrounds pose a particular problem in the analysis of paleoclimate (e.g. precipitation) time series (Schwarzacher, 1993). Statistical significance of spectral peaks was tested using a parametric approach (90%, 95%, and 99% false-alarm levels). The data were interpolated to an equal interval in wavelet analyses to detect non-stationary periodicities. In climate data, common features in wavelet power of two time series can occur, but at times can be merely a coincidence (Maraun and Kurths, 2004). We thus used cross-wavelet transform of our

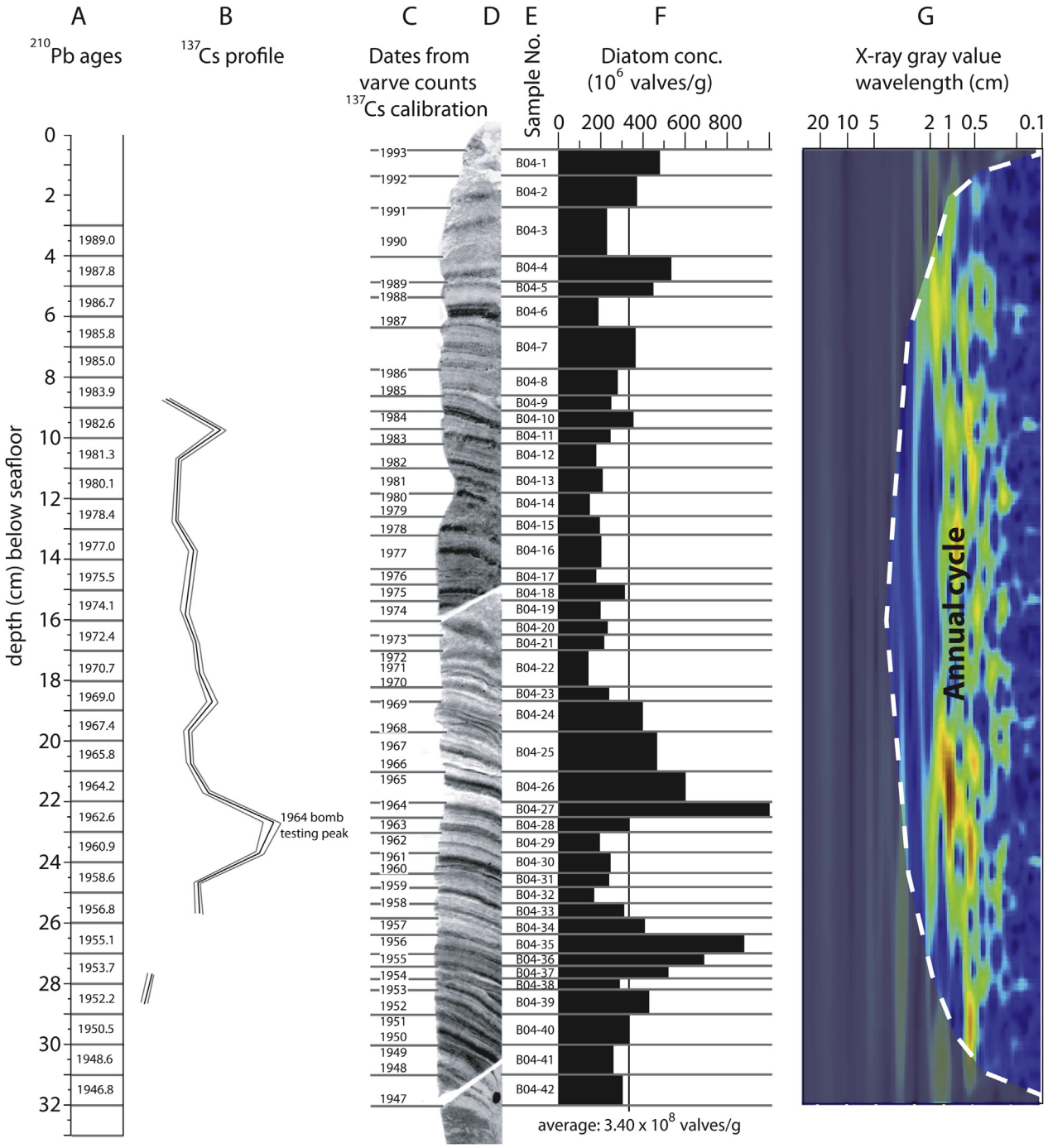

Fig. 3. Chronology, bulk sediment composition, total diatom abundance and wavelet analysis in the depth scale. (A) Age estimates based on ^{210}Pb results. (B) Decay profile of ^{137}Cs. Gray lines correspond to 1-sigma error. There was insufficient material to provide accurate ^{137}Cs dates above a depth of 8 cm, and at depths of 26–27 cm and 29–32 cm. (C) Calendar years assigned to varves by varve counting. A year is defined by the placement of the label beside the terrigenous lamina of each varve. Because the laminae are at an angle, the position of the year label for each varve corresponds to the varve expression along left edge of the X-radiograph image (i.e., the outer surface of the freeze core). From Chang (2004). (D) X-radiograph positive image of sediments. Lighter colored layers are diatomaceous laminae. Darker colored layers are terrigenous laminae. The left edge of the image represents the top surface of the freeze core, which experienced the least amount of shearing during coring. The 0.5-cm zone of severely sheared laminae has been removed from the right edge of the image. Diagonal gaps between slabs indicate where physical cuts were made. (E) Quantitative diatom sample labels. The delineations of the labels correspond to the varve expression along left edge of the x-radiograph image. Samples were sliced parallel to bedding planes. (F) Absolute diatom abundance per sample. (G) Wavelet scalogram of X-radiograph gray-scale values in depth domain (cm). Orange and yellow colors mark high wavelet coefficients (high spectral power or amplitude), and blue color marks low wavelet coefficients (low spectral power or absent amplitude) at specific wavelengths at specific locations. Gray areas bounded by the white dashed line delineates the cone of influence, which is the region of the wavelet spectrum where edge effects become important. (For interpretation of the references to color in this figure legend, the reader is referred to the web version of this article.)

data to identify and test the significance of common power using the Cross wavelet package in Matlab (Hudgins et al., 1993; Torrence and Compo, 1998; Grinsted et al., 2004; Maraun and Kurths, 2004). The data derived from the freeze core were compared to historical celestial records and instrumental ocean–atmosphere records. Celestial records include the sunspot cycle from 1947 to 1993, CRF over Climax, Colorado from 1953 to 1993, and solar irradiance (SI) from 1978 to 1993. These data were obtained from the National

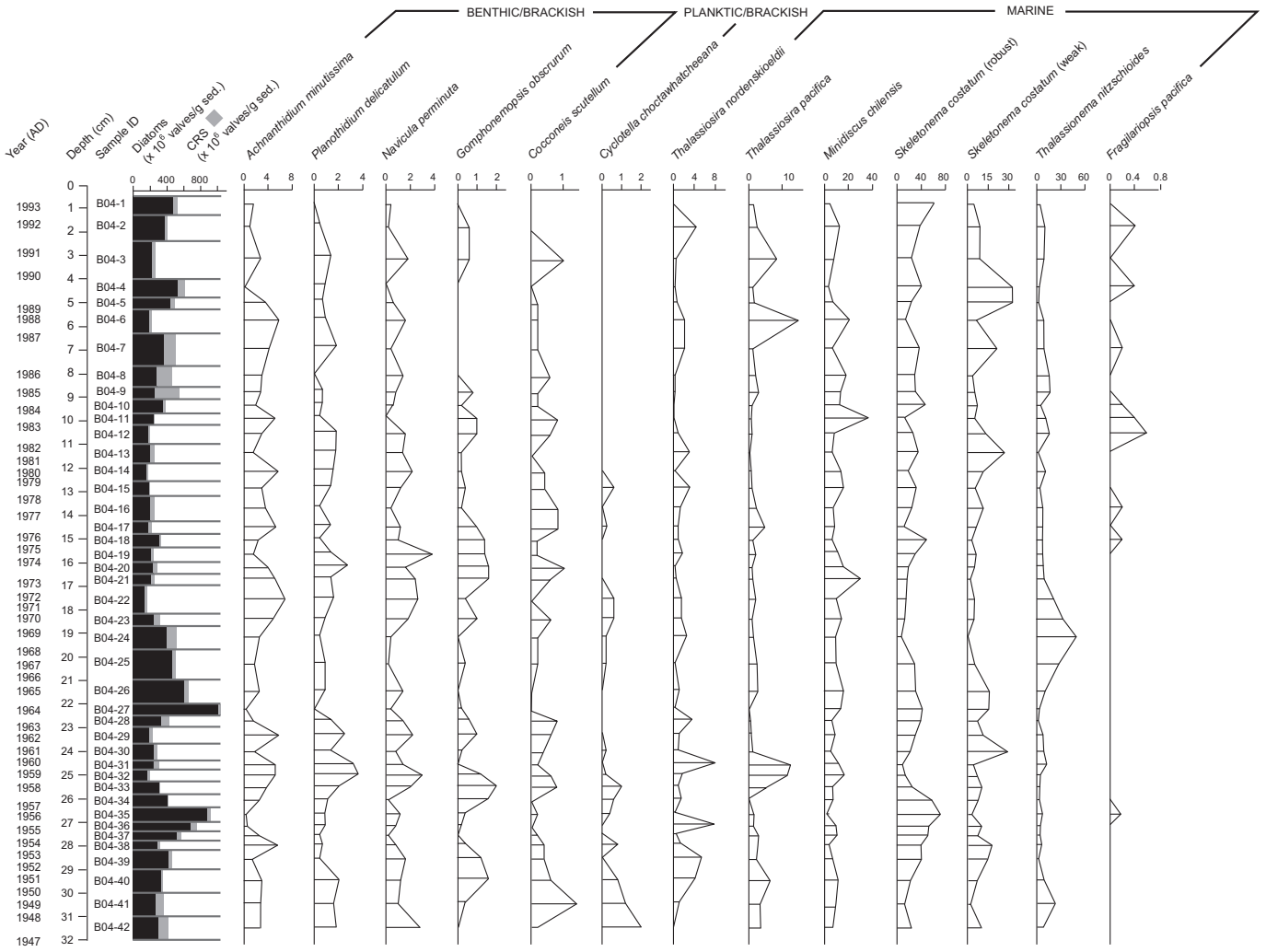

Fig. 4. Absolute abundance ($\times 10^6$ valves/g of dry sediment) of total diatoms and *Chaetoceros* resting spores (CRSs), and relative abundance (%) of individual diatom taxa.

Geophysical Data Center (NOAA; ftp://ftp.ngdc.noaa.gov/STP/SOLAR_DATA/). The CRF measured over Colorado is assumed to be representative of the northern hemisphere in general. SI and CRF were used only for graphical correlation and to calibrate the sunspot cycle in terms of solar irradiance fluctuation (Fig. 5).

Ocean–atmosphere records include mean annual precipitation (PPT), mean annual sea surface temperature (SST) and "spring" SST (average of April/May values), the mean annual Aleutian Low Index (ALI), and the mean annual North Pacific Index (NPI), and "spring" NPI (average of April/May values). Precipitation data were obtained from the National Climate Data and Information Archive (Environment Canada; http://climate.weatheroffice.gc.ca/climateData/canada_e.html) for locations on southwest Vancouver Island. Datasets from Bamfield (February 1903 to September, 1956), Bamfield East (August 1959 to December 1992), Bamfield West (October, 1955 to July, 1959), Kildonan (January, 1937 to May, 1976), Pachena Point (November, 1924 to February, 2007) and Tofino A (July, 1942 to December 2005) were compiled to complete the precipitation record. Sea surface temperature (SST) data were obtained from the Department of Fisheries and Oceans (Canada; http://www.pac.dfo-mpo.gc.ca/science/oceans/data-donnees/index-eng.htm) for lighthouse station Amphitrite Point on southwestern Vancouver Island. ALI data were obtained from the Department of Fisheries and Oceans (Canada; http://www.pac.dfo-mpo.gc.ca/science/species-especes/climatology-ie/cori-irco/indices/alpi.txt) and are described in Beamish et al. (1997). ALI measures the relative intensity of the Aleutian Low-pressure system over a given area of the north Pacific Ocean (from December through March, representing an average over one "year") and is expressed as an anomaly from the 1950–1997 mean. A positive index indicates a strong, or intensified, Aleutian Low, and a negative index indicates a weak low-pressure system. Subsequently, ALI can be used as a proxy for winter storminess in the north Pacific. NPI data were obtained from the National Center for Atmospheric Research, Climate Analysis Section (http://www.cgd.ucar.edu/cas/jhurrell/npindex.html). The periodicities of these data were also analyzed using a Discrete Fourier transform methodology.

5. Results

5.1. Chronology

Dating by counting varves starting at the year 1947 above the earthquake slump layer reveals that the youngest completely recovered varve represents the year 1992 (Fig. 3). The varve for 1993 is incomplete. The uppermost varves from 1994 to 1999 were not recovered, most likely because the sediments at the

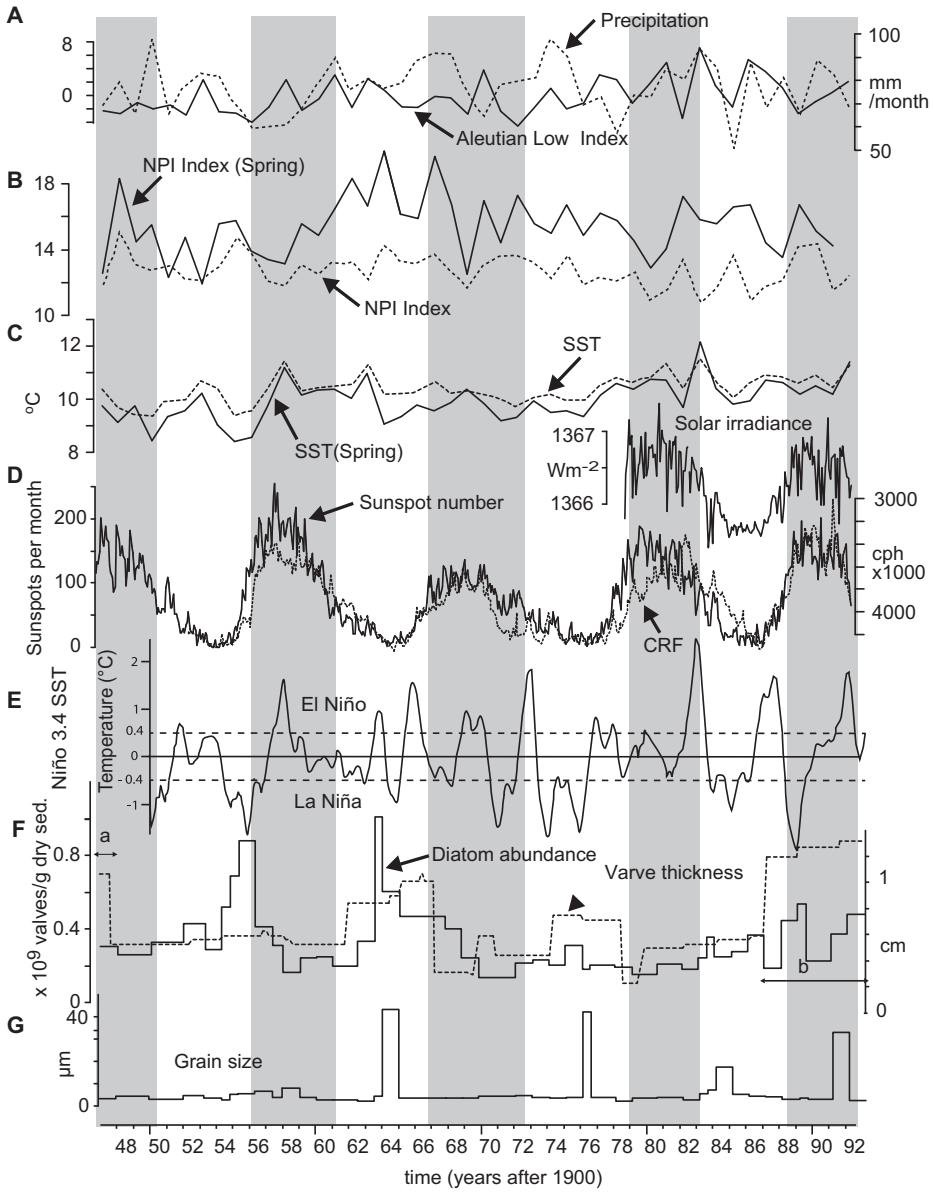

Fig. 5. Graphical representation of data used in this study. Instrumental data for (A) precipitation and Aleutian Low Index (ALI), (B) annual and spring North Pacific Index (NPI), and (C) annual and spring sea surface temperatures (SSTs). (D) Celestial datasets for number of sunspots per month, solar irradiance and counts per hour (cph) of cosmic rays. (E) Time series plots of the Niño 3.4 SST indices as five month running means using data from NOAA and relative to a base period climatology of 1950–1979. Values above thresholds of ±0.4 °C for Niño 3.4 are stippled to indicate ENSO events. The Niño 3.4 region is bounded by 120°W–170°W and 5°S–5°N (Trenberth, 1997). Data derived from sediment core for (F) diatom abundance and varve thickness, and (G) grain size. Intervals 'a' and 'b' in (F) were excluded from statistical analyses due to influence from the earthquake deposit and unsettled upper sediments, respectively. Gray bars highlight periods of high sunspot numbers.

sediment–water interface were too unconsolidated and water-saturated to adhere to the freeze corer surface. The years 1963 and 1964 were counted at a depth of 22–23 cm (Fig. 3). The ^{137}Cs profile corroborated this age, as a prominent peak representing the 1963–1964 peak in nuclear testing was found at a depth of 22.5 cm (Fig. 3).

The ^{210}Pb methodology provides reliable dates for sediments deposited during the past 150 years. Results from the ^{210}Pb analyses were converted into calendar years using the constant flux-constant sedimentation model (Fig. 3) and calibrated using background levels obtained from box cores from the western Vancouver Island margin just west of Barkley Sound (McKay et al., 2007). The constant flux-constant sedimentation model postulates that where there is a constant input of detrital material, there will also be a constant accumulation rate of ^{210}Pb to the bottom, where each sediment layer will have the same initial ^{210}Pb concentration (Sorgente et al., 1999). Assuming that no migration of ^{210}Pb has occurred in the sediment column, the ^{210}Pb concentration will decline exponentially with the cumulative dry mass of sediment. Sediment bulk density was not determined for TUL99B04, so an average dry bulk density of 2.275 g/cm^3 from adjacent correlative box core EFBC9703-2 from the inner basin (M. Hay, unpublished data) was used for the ^{210}Pb calculation. The ^{210}Pb results generally correlated well with age estimates based on varve counting throughout the core (Fig. 3A). The ^{210}Pb calendar year determined at the depth for 1963–1964 correlated well with the varve counts and the ^{137}Cs peak from nuclear testing (Fig. 3).

5.2. Sedimentology

X-radiographs of the laminated sediments display alternating dark and light banding typical of annually laminated hemipelagic sediments, where the dark laminae contain dense detritus and the light laminae contain porous diatom frustules (Fig. 3). Measured thickness of varves ranges from 0.4 to 1.31 cm. The mean thickness of the varves increases toward the top of the sediment column. The varves are thinner from 1947 to 1970, averaging 0.60 ± 0.14 cm/yr (1 − sigma standard deviation). From 1971 to approximately 1985, the varves average 0.63 ± 0.13 cm/yr in thickness. The uppermost varves from 1986 to 1992 average 1.06 ± 0.31 cm/yr and are not as well defined as the older varves. The progressive decrease in thickness toward the bottom signifies increasing sediment compaction and dewatering down-core, rather than increasing sedimentation rates toward the top of the core near the end of the 20th century. A sedimentation rate of 0.68 ± 0.23 cm/yr is calculated if all varves are taken into consideration.

Grain size distributions display distinct single-sample peaks at 1964, 1976, 1984 and 1992 (Fig. 5F). The average of these four peaks is 33.3 μm, whereas the average background value is 4.3 μm.

5.3. Diatom abundance

A total of 251 diatom taxa, not including resting spores, were identified from the samples. The major diatom species are listed in Appendix 3. The preservation quality (fragmentation and dissolution) of a variety of diatom morphologies was generally good, except for the delicate *Chaetoceros* spp. vegetative frustules.

The mean diatom abundance counted from the 42 samples is estimated at $3.40 \times 10^8 \pm 1.88 \times 10^8$ valves/g of dry sediment (Fig. 3). Diatom abundances are highest from 1954 to 1957 and from 1963 to 1969, with the highest abundance in 1956 (sample B04-35; 8.80×10^8 valves/g) and 1964 (B04-27; 1.01×10^9 valves/g). The lowest diatom abundance occurs from 1970 to 1972 (B04-22; 1.38×10^8 valves/g), with a recovery of diatom populations in the 1980s and a continued increase into the early 1990s. The mean *Chaetoceros* resting spore (CRS) abundance is estimated at $5.09 \times 10^7 \pm 5.57 \times 10^7$ valves/g, illustrating that *Chaetoceros* spp. is not a dominant taxon group in this system. Highest CRS abundance occurs in 1984 (B04-9; 3.13×10^8 valves/g) and the lowest occurs in 1978 (B04-15; 5.35×10^6 valves/g).

The total diatom abundance profile is dominated by fluctuations in the abundance of the robust form of *Skeletonema costatum*, a coastal spring and summer bloom taxon (Appendix 4; Fig. 4). Other dominant diatoms, all of which have concentrations greater than 1×10^8 valves/g are, in order of decreasing abundance, the cosmopolitan marine taxon *Thalassionema nitzschioides*, the weakly silicified form of *Skeletonema costatum*, and the early spring bloom diatom *Minidiscus chilensis* (Fig. 4).

Several taxa have noticeable trends. The brackish water, planktic estuarine diatom *Cyclotella choctawhatcheeana* has its greatest abundance at the bottom of the laminated section, prior to the mid-1960s. The abundance of this diatom then decreases until none are observed after ~1980. Benthic brackish water taxa, such as *Cocconeis scutellum*, *Gomphonemopsis obscurum*, *Navicula perminuta* and *Planothidium delicatulum*, show similar relative abundance trends through time, suggesting that these taxa responded similarly to environmental conditions or were being similarly diluted by more dominant taxa.

A newly described diatom, the sub-arctic to temperate oceanic taxon *Fragilariopsis pacifica* (Lundholm and Hasle, 2010; Chang et al., 2013), which features prominently in Effingham Inlet sediment trap samples during the cold La Niña spring and summer of 1999 (Chang et al., 2013), has insignificant relative abundances of <0.6% throughout the freeze core record (Chang, 2004; cf. Patterson and Fishbein, 1989). This taxon appeared during the cool period of 1956, but not during the 1974–1976 cool interval, and occurred more frequently after the mid-1970s during brief cool phases of the PDO. The spring bloom taxa *Thalassiosira nordenskioedlii* and *Thalassiosira pacifica* have punctuated abundance maxima and do not appear to have any trend throughout the study interval (Fig. 4).

5.4. Statistical analyses

Using wavelet analysis, significant cycles have been detected in the sediment gray-scale value, grain size and absolute diatom abundance. Wavelet analysis of sediment gray-scale values reveals annual cycles of 0.3–~1.5 cm thickness, giving a mean sedimentation rate of 0.61 cm/yr (Fig. 3). These values are similar to the thickness and rate calculated using physical measurements of varve thickness, demonstrating that the automated computer scans and manual inspection of the varves detected the same visual cues.

In diatom abundance, significant cycles occur at ~11 years in the time domain (Fig. 6A and B). For the *S. costatum* data there is a strong ~9–12 year cyclicity dominating the record prior to the mid-1970s and becoming less intense in the latter part of the record (Figs. 7A and 8A). As three complete cycles were detected in several proxies (grain-size, diatom concentration, *S. constatum* relative abundance and varve thickness), bandwidth uncertainty associated with the ~11 year cycle is low [Figs. 6–8]. The *S. costatum* data also displays a strong non-stationary ~2–3-year cycle beginning in the 1980s (Figs. 7A and 8A). The weakly silicified variant of *S. costatum* data is characterized by a non-stationary ~2–3- year cyclicity in the latter part of the record (Figs. 7B and 8B).

The grain size data is dominated by a series of non-stationary cycles centered on the 1970s that correlate with cycles of ~4 years, ~8 years and a weaker 9–12 year band (Fig. 6C). An ~3 year grain-size cycle occurs only in the 1970s (Fig. 6C).

For the total annual precipitation data there is a very strong non-stationary ~7-year cycle dominating the record after the mid-1970s as well as an ~2-year cycle developing in the 1980s (Figs. 7C and 8C). For April to June precipitation, which coincides with times of maximum upwelling and diatom growth, there are strong ~2–3-year cycles dominating the record beginning in the 1980s (Figs. 7D and 8D).

Cross-wavelet analysis between precipitation and the two *S. costatum* variants resulted in recognition of several non-stationary correlations. Cross-wavelet analysis between total precipitation and *S. costatum* was characterized by a non-stationary short-lived ~7-year cycle that prevailed in the late 1950s and early 1960s (Fig. 9A). Following this, there was a major wavelength shift in the early 1960s to an ~9–11 year cycle that then gradually transitioned in the mid-1970s to ~7–10 year cycle. A short-lived non-stationary 2–3 year cycle developed in the early 1980s (Fig. 9A). Cross-wavelet analysis between April–June precipitation and *S. costatum* resulted in recognition of an ~ 8–12 year cycle that developed in the mid 1950s and faded out in the early 1970s (Fig. 9B). The early 1980s was characterized by a short-lived 2–3 year cycle (Fig. 9B).

Cross-wavelet analysis between total precipitation and the weakly silicified variant of *S. costatum* resulted in recognition of a non-stationary ~7–9-year cycle that developed in the mid-1970s (Fig. 9C). Cross-wavelet analysis between April–June precipitation and the weakly silicified variant of *S. costatum* was characterized by a short-lived 2–3 year cycle in the early 1980s (Fig. 9D) that was

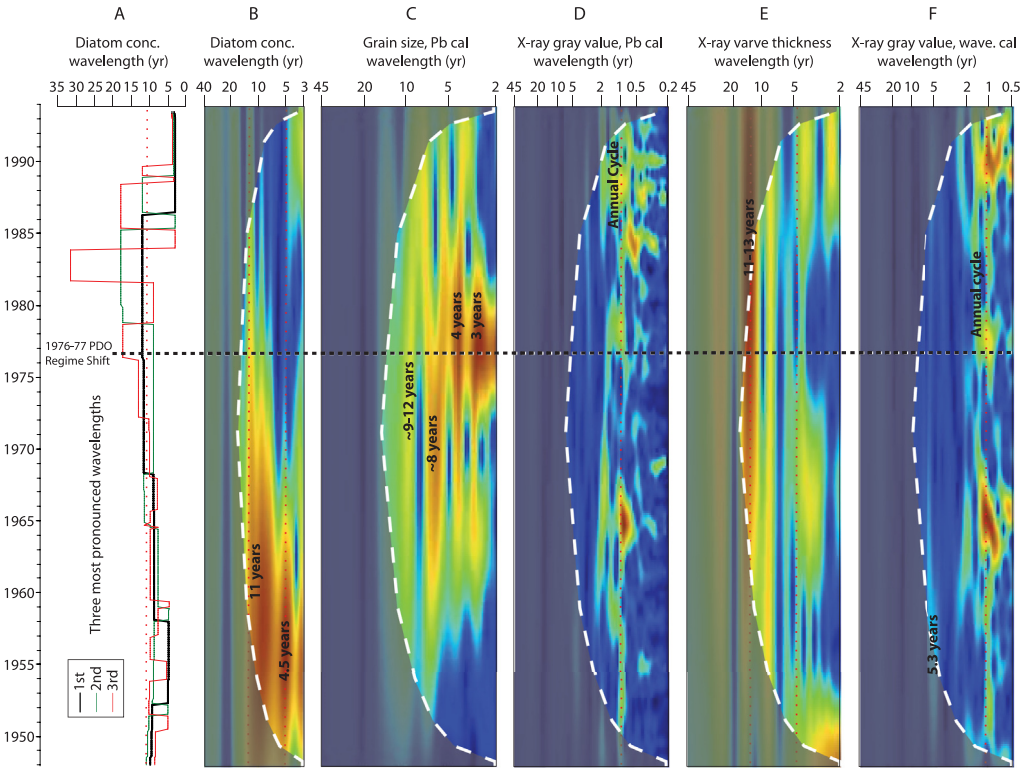

Fig. 6. Wavelet scalograms in the time domain. Scalogram axes represent the logarithmic scaled period (or wavelength). Black horizontal line across diagram denotes 1976–1977 PDO regime shift. See Fig. 3 for explanation of scalogram colors. (A) Three most pronounced (strongest local wavelet coefficients) periods in diatom abundance. Dotted line denotes the 11-year cycle. (B) Wavelet scalogram of diatom abundance. (C) Wavelet scalogram of grain-size data. (D) Wavelet scalogram of X-radiograph sediment gray-scale values using the ^{210}Pb date as the basis for the age model. (E) Wavelet scalogram of X-radiograph of varve thickness (analyzed from image in Fig. 3B). (F) Wavelet scalogram of X-radiograph sediment gray-scale values using the varve count/wavelet transform (as described by Prokoph and Patterson, 2004a,b). (For interpretation of the references to color in this figure legend, the reader is referred to the web version of this article.)

very similar to that observed with *S. costatum* (Fig. 9B). There is evidence of a stationary ~7 year cycle may have developed in the mid-1980s but as it mostly falls outside the cone of influence it may be an artifact (Fig. 9D). Linear (Pearson) correlation indicates that there are significant negative correlations between sunspot numbers and spring NPI, precipitation, and varve thickness (Table 2, Fig. 5). There is also a one-year lag in correlation between sunspot numbers and diatom abundance when diatom abundance is transformed to the time domain (Table 2). The ~11-year sunspot cycle correlates well with direct measurements of solar irradiance (Veizer, 2005; Fig. 5D). For the 11-year cycle band, an amplitude of ~60 sunspots per month is comparable to amplitudes of 1.4 W/m^2 in solar irradiance and ~260,000 counts per hour of CRF (Fig. 5D). Neither the mean annual ALI nor NPI are correlated with sunspot numbers from 1947 to 1993 (Table 2, Fig. 5). If the data are grouped into "low sunspot number" and "high sunspot number" at a threshold of 82.5 sunspots/month (sample mean for the time interval studied) for analysis of variance (ANOVA), the relation between solar variability versus climate, diatom abundance, varve thickness and grain size becomes more robust and less affected by the possible influence of extreme values (Table 1). Thicker varves and higher diatom abundance (with a one-year lag) are correlated with low sunspot numbers at >99% confidence ($p < 0.01$). This correlation does not hold true in interval 'b' defined from Fig. 5F, especially for varve thickness. Discrete Fourier transform and spectral analysis highlight that the 11-year periodicity is the most significant (>90% confidence) for sunspot cycles, diatom abundance and varve thickness but not for grain size and ocean–atmosphere records (Fig. 10). The response of diatom productivity to the change in solar irradiance is likely delayed by ~1 year (Tables 1 and 2), possibly due to a lagging response of the ocean–atmosphere system to external drivers. Moreover, varve thickness is significantly increased during years with low sunspots, particularly for years centered on 1964 and 1976 (Fig. 5) due to the increase in abundance of the chain-forming diatom *Skeletonema costatum* (Fig. 4), signifying that the thicker varves during these years are a result of enhanced primary productivity. The possible presence of large numbers of *Skeletonema costatum* chains could result in an increase in grain-size during those same years (Fig. 5F). Increased varve thickness in 1992 is considered to be the effect of unsettled sediment at the top of the record.

Table 2
ANOVA of climate, diatom and sedimentary data versus sunspot numbers.

Group	Means <82.5 SPY[a]	Means >82.5 SPY	*p*-Value
ALI	0	−0.32	0.69
NPI (spring)	15.78	15.05	0.178[c]
NPI	12.73	12.67	0.83
SST (°C)	10.27	10.49	0.164[c]
SST (spring) (°C)	9.78	10.14	0.091[c]
Precipitation (mm/month)	80	73	0.041[d]
Grain size (μm)	7.3	5.5	0.45
Diatom abundance (valves/g)	3.44×10^9	2.89×10^9	0.21
Diatom abundance (1YS[b]) (valves/g)	3.72×10^9	2.56×10^9	0.008[d]
Varve thickness (cm)	0.65	0.50	0.002[d]

[a] SPY = sunspots per year.
[b] 1YS: 1 year shifted.
[c] Difference in low/high SPY at >80% confidence.
[d] Difference in low/high SPY at >95% confidence.

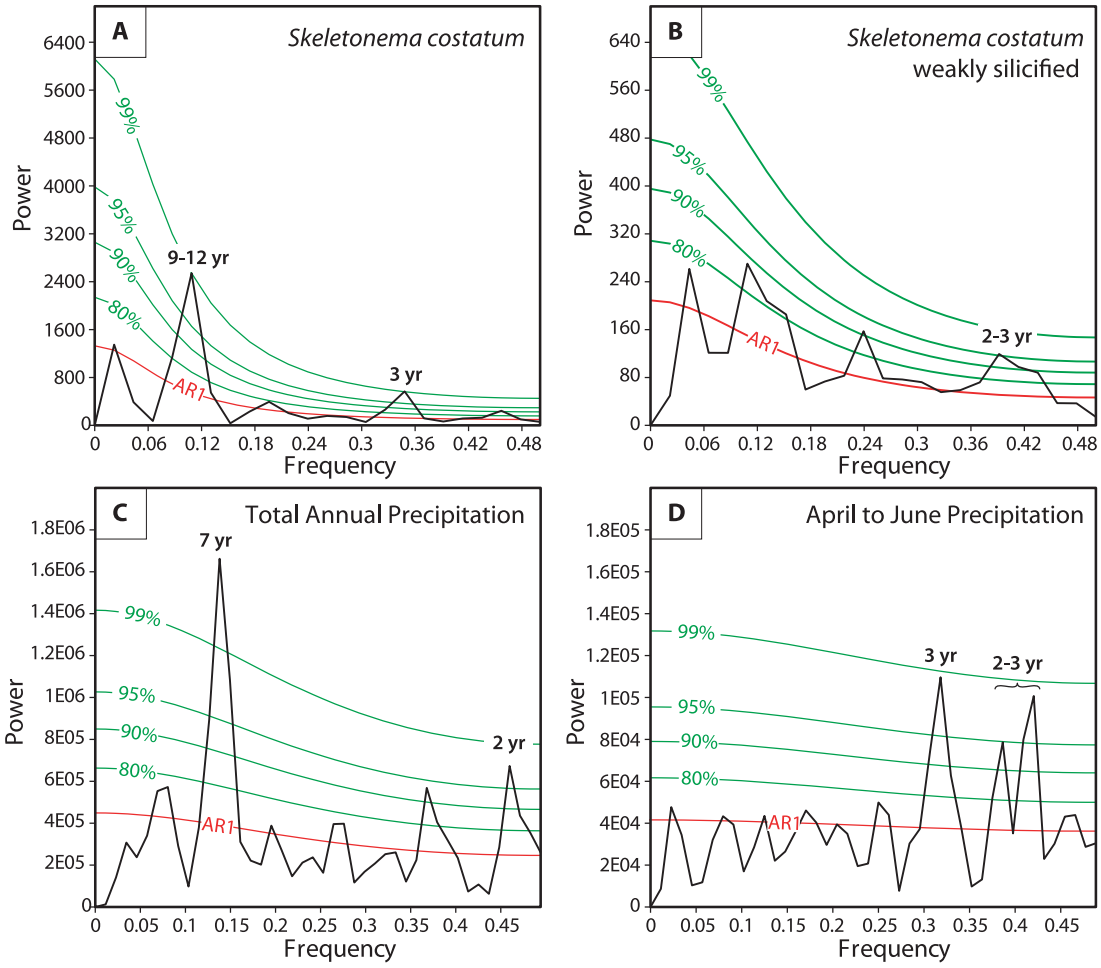

Fig. 7. REDFIT spectral analysis. (A) *S. costatum*. (B) Weakly silicified *S. costatum*. (C) Total annual precipitation. (D) April to June precipitation. Peaks above the 95% confidence interval are considered statistically robust.

6. Discussion

Wavelet and spectral analyses have revealed prominent cyclicity displayed in sedimentary gray-scale values, varve thickness, total diatom concentration, abundance data for both *S. costatum* variants, grain size and precipitation. The 2–3, ~4.5, and 7-year cycles in total diatom and *S. costatum* concentrations, and total and April to June precipitation can be attributed to ENSO cyclicity. The 9–12 year cycles in sedimentary gray-scale, varve thickness, *S. costatum* concentration and precipitation correlate with the Schwabe sunspot cycle. These results demonstrate that diatom productivity, and the resulting sedimentation pattern, are affected not only by large-scale ocean–atmosphere perturbations, but also by solar forcing on scales other than the annual cycle. The response of the diatoms to the sunspot cycle is further consistent with recent findings that solar activity directly impacts ozone production and indirectly influences cloud formation, which collectively have a significant impact on atmosphere–ocean circulation, thus amplifying the relatively weak solar activity fluctuation throughout a 11-year solar cycle (Meehl et al., 2009; Gray et al., 2010). Resultant changes to the jet stream trajectory during a sunspot cycle influences weather systems and upwelling patterns in the NE Pacific, which seems to not only impact phytoplankton productivity and sedimentation patterns at the Schwabe sunspot cycle as observed in this short record but over long (millennial) time scales as well (Patterson et al., 2004, 2007). Prokoph et al. (2012) recognized a similar 11-year cyclicity in mean annual stream flow data from sites across southern Canada, including the outlet of the Chilliwack River on the British Columbia mainland. Also observed was a significant 2–8-year and a >20-year cyclicity that was attributable to ENSO and PDO, respectively.

Cyclical ENSO patterns have also been detected from other areas in the northeast Pacific Ocean. Tabata (1989) found that the most common periods for interannual variability are 2.5 and 6–7 years in the northeast Pacific, based on long-term studies of ocean properties. This interannual variation is attributable to a westward propagation of baroclinic Rossby waves that are often associated with ENSO teleconnections (Tabata, 1989). Haigh et al. (1992) reported that there was a 7-year toxicity cycle for dinoflagellates in coastal British Columbia and attributed the cyclicity to ENSO. Dean et al. (2004) recognized similar 4–8 year cycles based on analysis of detrital volcanic debris washed into the Gulf of California by riverine flow that were attributed to ENSO. McQuoid and Hobson (1997) saw that *Skeletonema costatum* had a ~4-year cycle in abundance in Saanich Inlet in which high numbers of this taxon occurred during warm ENSO cycles. In Effingham Inlet, because *S. costatum* is the most abundant species and dictates the total diatom abundance profile from which the ENSO cycle was detected, we can also infer that ENSO cyclicity affects the abundance of *S. costatum* in this inlet.

An analysis of the X-radiographs and wavelet scalograms shows that the annual cycle of sedimentation is continuous and persistent

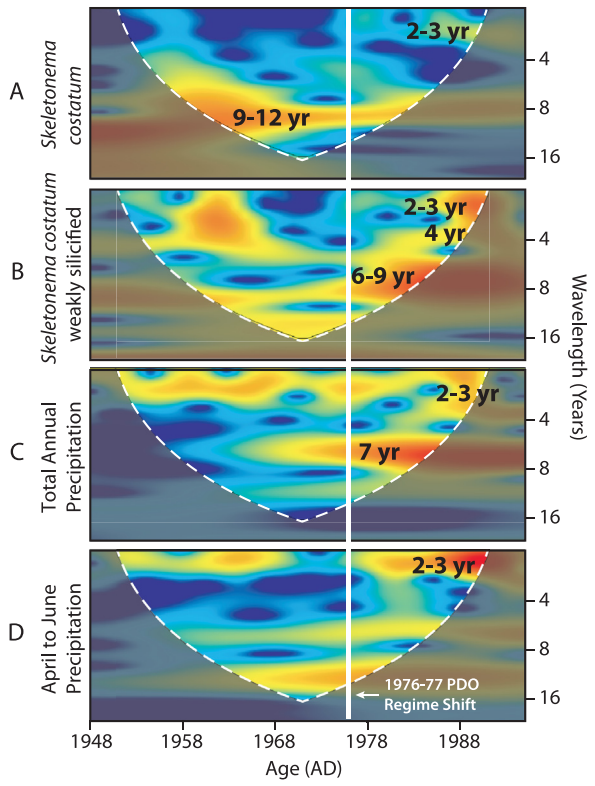

Fig. 8. Wavelet scalograms in the time domain for *Skeletonema costatum* and precipitation. Vertical axes represent the logarithmic scaled period (or wavelength). White vertical line across diagram denotes 1976–1977 PDO regime shift. See Fig. 3 for explanation of scalogram colors. (A) Relative abundance of *S. costatum*. (B) Relative abundance weakly silicified *S. costatum*. (C) Total annual precipitation (mm). (D) April to June precipitation (mm). (For interpretation of the references to color in this figure legend, the reader is referred to the web version of this article.)

throughout the late 20th century. Based on total diatom abundance, the 2–7 year ENSO cycle was detected by wavelet analysis and appears to be most prominent from 1947 to the mid-1960s (red and orange colors) when diatoms were the most abundant, and then less prominent from the mid-1960s to 1970s (blue colors) when diatoms were the least abundant, and more prominent again from the mid-1980s onwards when the diatom abundance recovered (Figs. 4, 6 and 7). ENSO cyclicity on the sediment gray-scale value scalogram shows similar results where the cyclicity is particularly prominent from 1947 to the early 1970s (Fig. 6D). Through the duration of the 1947–1993 Effingham Inlet record, Whitney and Welch (2002) suggest that El Niños strong enough to significantly influence marine productivity only occurred during the 1957–1958 and 1982–1983 events. The warmer SSTs that prevail during an El Niño also suppresses the upwelling of nutrients, which in turn correlates with lower diatom abundances in the Effingham Inlet record during the 1957–1958 and 1982–1983 El Niños. Lower diatom abundances also occur in the Effingham Inlet record that correlate with the strong El Niño events of 1969, 1987, and 1991 (Gergis and Fowler, 2009). The only strong El Niño event absent from the Effingham Inlet diatom record is the 1964 event, suggesting that most strong El Niño events will have an influence on productivity along the BC coast.

There is a link between ENSO and PDO, as the PDO either amplifies or suppresses the influence of ENSO events (Biondi et al., 2001). The impact of this association is widespread, affecting not only precipitation and temperature but a host of parameters including wind, stream flow, snow pack and storm surge (e.g. Fleming and Clark, 2005; Stahl et al., 2005). In western North America, El Niño events become more intense during positive phases of the PDO due to the deepening of the AL (Trenberth and Hurrell, 1994; Ware and Thomson, 2000). Our observations of generally lower diatom abundances since the 1976–1977 regime shift appear to corroborate this. Newman et al. (2003) have presented evidence that PDO variability from interannual to decadal time-scales is related to a combination of direct ENSO forcing, a return to more normal North Pacific SSTs in post-ENSO years and random atmospheric signals. In our record, the 11–13 year sunspot cycle is most prominent from 1947 to the early 1980s (red to yellow colors) and remains relatively strong throughout the length of the laminated section, as indicated by both the diatom abundance, *S. costatum*, sediment gray-scale value, cross wavelets between total precipitation and *S. costatum*, and cross wavelets between April to June precipitation and *S. costatum* scalograms (Figs. 6B,C, 8A,B and 9A,B). The correlation is most dominant in the diatom record prior to the mid-1970s, when diatoms were more abundant, and then becomes stronger in the gray-scale record.

According to the correlations derived from the freeze core and the environmental records, years of low solar activity and increased CRF to the lower atmosphere (i.e., increased cloudiness) is correlated to increased precipitation, an intensified NPH during spring that can lead to intensified upwelling, and increased diatom productivity along the west coast of Vancouver Island. Although Christoforou and Hameed (1997) suggest that during low sunspot years the AL moves closer to the North American coast, which generally suggests downwelling and more winter-like conditions along the coast, we postulate that the increased cloud cover during sunspot minima suppresses the intensity of the AL, in particular during April/May when the solar irradiance rises in the northern hemisphere. A suppressed AL during the spring could allow the NPH system to move closer to the Vancouver Island region earlier than usual, thus providing an early shift in the year from a downwelling to an upwelling regime. In particular, significantly increased precipitation during low sunspot years ($p = 0.041$) is an indicator of increased cloudiness. Thus, the link between solar cycles, northeast Pacific climate and primary productivity is most closely linked to atmospheric pressure systems during April/May (e.g. Hickey, 1998; Ware and Thomson, 2000; Patterson et al., 2011). In an analysis of a 62-year-long, ~4400-year-old section from elsewhere in the inner basin of Effingham Inlet, Chang and Patterson (2005) observed a major sedimentological shift. They concluded that their sedimentological patterns and observed changes in diatom assemblages were related to a change in the relative intensities of the AL and NPH. Similar to the scenario described for the freeze core, Chang and Patterson (2005) hypothesized that the observed thicker diatomaceous varves at the bottom of the section reflected deposition influenced by a stronger NPH system with associated coastal upwelling and enhanced diatom production. This situation is similar to modern annual spring and summer production observed from sediment trap studies within the inner basin (Chang et al., 2013). Contrarily, thinner silty varves at the top of the section were interpreted as indicative of increased AL influence, resulting in greater amounts of precipitation and reduced upwelling, a scenario similar to modern autumn conditions within the inlet (Chang et al., 2013).

In the freeze core record, cyclic variation in grain size becomes very prominent at several non-stationary cycle wavelengths during the mid-1970s. These cycles may be related to the 1976 Pacific climate shift, which occurred when the PDO index shifted from dominantly negative values (cool conditions) for the period from 1951 to 1975 to dominantly positive values (warm conditions) for the period from 1977 to 2001 (Mantua et al., 1997; Mantua and

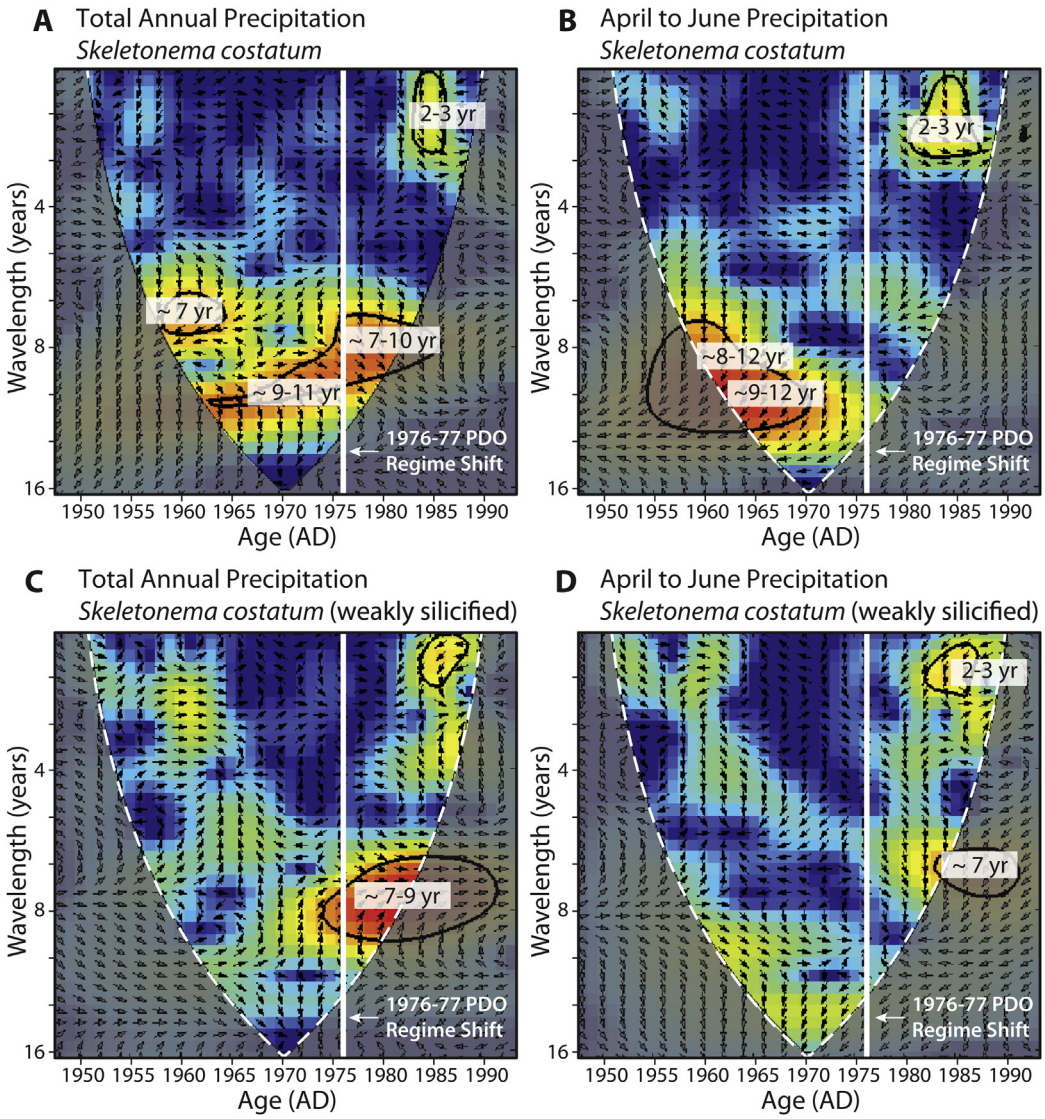

Fig. 9. Cross-wavelet transformations. See Fig. 3 for explanation of colors. White vertical lines denote 1976–1977 PDO regime shift. (A) Total annual precipitation (variable 1) and *S. costatum* (variable 2). (B) April to June precipitation (variable 1) and *S. costatum* (variable 2). (C) Total annual precipitation (variable 1) and weakly silicified *S. costatum* (variable 2). (D) April to June precipitation (variable 1) and weakly silicified *S. costatum* (variable 2). Relative phase relationships are shown as arrows with in-phase pointing right, anti-phase pointing left, variable 1 leading variable 2 pointing up and variable 2 leading variable 1 pointing down. Apparent phase relationships may be subject to error introduced by comparing calendar-derived precipitation data against geologically derived (^{210}Pb, ^{137}Cs and varve counting) *S. costatum* data. The enclosed black curves indicates 95% significance against a red-noise background. (For interpretation of the references to color in this figure legend, the reader is referred to the web version of this article.)

Hare, 2002; Hartmann and Wendler, 2005) The impact of the shift through the north Pacific region is variable and was marked by a series of anomalous winter (Namias, 1978). In Alaska, cloudiness, wind speeds and precipitation amounts increased while mean sea level pressure and geopotential heights decreased during the positive phase (Hartmann and Wendler, 2005). In contrast, in coastal areas of British Columbia the 1976 shift to a positive PDO resulted in milder and dryer winters (British Columbia Ministry of Water, Land and Air Protection, 2002). Along the southwest coast of Vancouver Island, the compiled instrumental records show there was an overall 6.1% decrease in precipitation following the 1976 regime shift with a decrease of 8.9% during the winter December–February interval. As the 1976–1977 shift to a positive PDO phase became established, the significance of grain-size cyclicity in the Effingham Inlet freeze core record diminished, and a 9–12 year cyclicity in *S. costatum* relative abundance disappeared (Fig. 8A). The mid-1970s shift from diatom concentration (Fig 6B) to varve thickness (Fig. 6E) dominating the observed 11-year cyclicity may also be related to the PDO regime shift. The grain size peaks in 1964, 1976 and 1984 visually correlate with some intervals of low sunspots (Fig. 5F). There is no peak during the low sunspot interval from 1953 to 1954, although there is a peak in the unconsolidated sediments of 1991, which was an interval of high sunspots. Had grain size peaks appeared consistently during years with low sunspots, a relationship could have been drawn that would have suggested that an increase in diatom production during times of low sunspots influenced the grain size (i.e., larger or more chain-forming diatom taxa). However, spectral analysis reveals that there is no 11-year sunspot cycle recorded in grain size fluctuations (Fig. 10). There is a moderate correlation between grain size and varve thickness (Table 2). Chang and Patterson (2005) have shown that varve thickness is governed mainly by the thickness of the spring/summer diatomaceous lamina, and not an increase in grain size due to increased detrital input. The abundance of benthic diatoms could

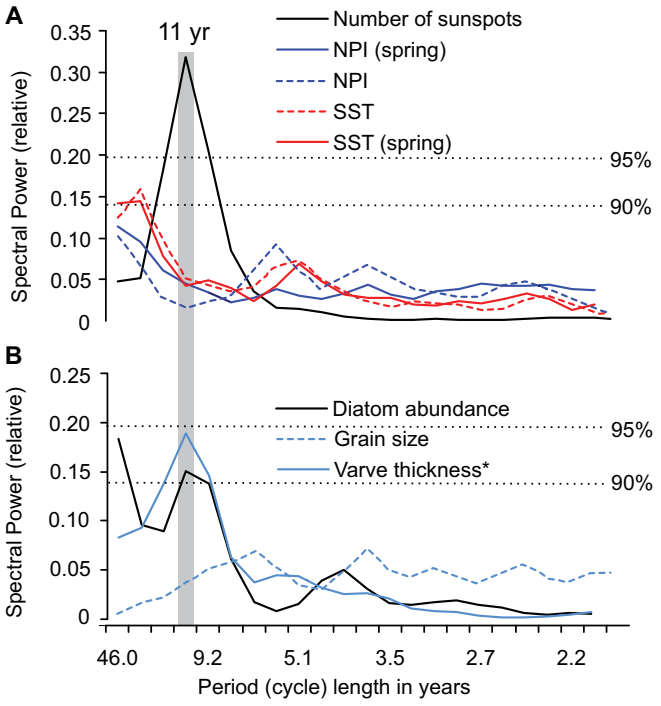

Fig. 10. Spectral analysis using a fast Fourier transform with a 5-lag Hamming window, and 90% and 95% confidence limits from an *F*-test. (A) Sunspot number and ocean–atmosphere data. (B) Diatom and sedimentary data. Asterisk indicates that top- and bottom-most varve thickness data (see Fig. 5F) were replaced by mean values. Gray bar highlights the 11-year period.

be used as a proxy for precipitation-induced runoff from shallower environments in which such species live. Sediment trap studies from within Effingham Inlet show that most benthic diatoms are deposited to the basin during the autumn and winter, when precipitation is at a maximum (Chang et al., 2013). Coarser grain size during the autumn and winter was also inferred geochemically (increased Ti/Al ratios), but direct grain size measurements on lithogenic materials were not made. Thus, the more or less uniform thickness of the detrital laminae (Fig. 3D) throughout the 1947–1992 record suggests that the grain size peaks derived in this study could instead be influenced by the types of planktic diatoms present in the diatomaceous laminae. For example, *Skeletonema costatum*, an upwelling-sensitive diatom that blooms in great numbers during the spring and summer, dominates all species identified in this study (Appendix 4). Although *S. costatum* is small in diameter, it is a colonial, chain-forming species. It is possible that clumps or mats of intertwined chains were not fully disaggregated during the sonication process, leading to anomalous increases in grain size. Furthermore, the types of wavelet and spectral analysis used in this study, i.e., continuous wavelet transform with Morlet wavelet and Fourier transform, respectively, are well-suited for gradually changing signals, but the abrupt changes in grain size variability (Fig. 5F) may be insufficiently detected by these methods. That said, the relative abundance of *S. costatum* has peak maximum relative abundance peaks in the years centered around 1956 and 1964, 1976, 1984 and 1993 (Fig. 4), corresponds with low sunspot numbers (Fig. 5D). Spectral analysis also shows an 11-year cycle in diatom abundance, *S. costatum* relative abundance and varve thickness. Although a time lag of one year exists between diatom concentration and the sunspot cycle cycles derived from other proxies, including grain size, varve thickness and partially linked *S. costatum* relative abundance show a clear correlation with the sunspot cycle and ENSO. Cross-wavelet analysis between *S. costatum* and total precipitation and April to June precipitation also shows a ~9–11 and ~8–12-year correlation prior to the 1976 regime shift, which breaks down with the development of positive PDO conditions (Fig. 9A,B). These results suggest that an underlying cyclicity exists and is inherent within the pattern of sedimentation. Accurate annual subsampling on a longer time scale is needed for a more robust correlation between primary productivity, climate and solar forcing.

Cycles evident in gray-scale, diatom abundance patterns and cross-wavelet results between *S. costatum* and precipitation show a clear relationship to the 11-year Schwabe sunspot cycle, indicating that sunspot activity and its effects on the troposphere ultimately drive Pacific atmosphere–oceanographic changes (e.g. Gray et al., 2010), effects of which are eventually recorded in the sedimentary record. The sedimentological expression of the sunspot cycle is strongly controlled by the phases of the PDO as correlations with solar cyclicity largely disappear in the Effingham Inlet record at the 1976–1977 climate regime shift. A longer record is required to test whether the high levels of confidence can be maintained in older sediments, although evidence of the Gleissberg cycle, has been reported in longer Late Holocene records from Effingham Inlet (Patterson et al., 2004, 2005) and anoxic basins within the Seymour-Belize Inlet Complex further north on the mainland British Columbia coast (Patterson et al., 2007). We also know that the ~11-year cycles observed in Effingham Inlet cannot be explained by other phenomena such as tidal cycles (cf. Berger et al., 2004; Berger, 2010). Hence, a decrease of ~1.4 W/m^2 in solar irradiance and 4% decline in solar ultraviolet radiation through a sunspot cycle is amplified by a positive feedback mechanism with low altitude cloud formation and the suppression of the AL during spring. This leads to the enhanced influence of the spring NPH and early seasonal upwelling with an approximate four-fold increase in diatom production during years of low sunspots. Other ocean–atmosphere oscillations such as the PDO (Biondi et al., 2001; Chavez et al., 2003), the Quasi-Biennial Oscillation (Labitzke, 2003), and ENSO have a more direct and stronger influence on climate and therefore marine productivity along the coast of Vancouver Island, although these oscillations themselves may also be modulated by solar activity (e.g. Shen et al., 2006). Solar irradiance variability thus represents an important driver of short-term climate and marine primary productivity. Such a mechanism will provide a new pathway for ocean–climate modeling, in addition to more traditional modeling methods.

7. Conclusions

An AD 1947–1993 record of annually deposited laminated diatomaceous sediments from anoxic Effingham Inlet archives ~2–3, ~4.5, ~7 and ~9–12-year cycles in the diatom record and ~11–13 year cycles in the sedimentary varve thickness record. These results suggest that both the quasiperiodic 2–7 year ENSO and 11-year Schwabe sunspot cycle had an influence on primary productivity and sedimentation patterns. A strong cyclic peak in the grain-size data corresponding to the mid-1970s may be correlated to the well-documented 1976–1977 northeast Pacific regime shift, when the PDO index went from negative to positive. The occurrence of higher spring (April/May) values for the North Pacific High pressure index through this interval suggests that there was both a suppression of the influence of the Aleutian Low and an increase in cloud cover during this time. These concomitant changes resulted in enhanced coastal upwelling, occurring earlier in the year, which stimulated diatom production. This research suggests that the Schwabe sunspot cycle, intensified by cloud cover and modifications in the upwelling regime, has a major influence on primary

productivity in the northeast Pacific region. The development of positive or negative phases of PDO has a major influence on the expression of both Schwabe solar cycles and ENSO in the sediments of Effingham Inlet. ENSO displays a very different period that varies according to the parameter measured, during the cool PDO conditions that existed prior to 1976–1977 and the warm conditions that prevailed after. The phase of PDO similarly impacts the expression of 9–12 year Schwabe solar cycles, as they dominated the Effingham Inlet record during the negative PDO conditions that existed prior to 1976 and were suppressed during the following positive phase.

Acknowledgments

We thank the crew of the CCGS *John P. Tully*, and the researchers and staff at the Pacific Geoscience Centre and the Institute of Ocean Sciences in Sidney, British Columbia, Canada for core recovery and technical assistance. The Geological Survey of Canada (Ottawa) is thanked for the use of their X-ray facility. This research was funded by a strategic project grant from the Natural Sciences and Engineering Research Council of Canada (NSERC) and a Canadian Foundation for Climate and Atmospheric Sciences (CFCAS) grant to RTP, and by grants from the Cushman Foundation for Foraminiferal Research and the Geological Society of America student research program to ASC. We thank Gill Alexander (QUB), Carley Crann (Carleton) and Becki Montsion (Carleton) for cartographic support and John MeNeely (QUB) for carrying out the grain size analysis. The paper benefited considerably from the thoughtful comments of Jason Addison (USGS) and an anonymous reviewer.

Appendix A. Supplementary material

Supplementary material related to this article can be found at http://dx.doi.org/10.1016/j.quaint.2013.02.001.

References

Beamish, R.J., Neville, C.E., Cass, A.J., 1997. Production of Fraser River sockeye salmon (*Oncorhynchus nerka*) in relation to decadal-scale changes in the climate and the ocean. Canadian Journal of Fisheries and Aquatic Sciences 54, 543–554.

Berger, W.H., 2010. On glacier retreat and drought cycles in the Rocky Mountains of Montana and Canada. Quaternary International 215, 27–33.

Berger, W.H., Schimmelmann, A., Lange, C.B., 2004. Tidal cycles in the sediments of Santa Barbara Basin. Geology 32, 329–332.

Biondi, F., Gershunov, A., Cayan, D.R., 2001. North Pacific decadal climate variability since 1661. Journal of Climate 14, 5–10.

Blais-Stevens, A., Clague, J.J., Bobrowsky, P.T., Patterson, R.T., 1997. Paleoseismic evidence in late Holocene sediments, Saanich Inlet, British Columbia. Canadian Journal of Earth Sciences 34, 1295–1420.

Blais-Stevens, A., Patterson, R.T., 1998. Foraminiferal biofacies of Saanich Inlet, Vancouver Island, British Columbia: valuable environmental indicators. Journal of Foraminiferal Research 28, 201–219.

British Columbia Ministry of Water, Land and Air Protection, 2002. Indicators of Climate Change for British Columbia 2002. British Columbia Ministry of Water, Land and Air Protection. http://www.gov.bc.ca/wlap, 48 p.

Chang, A.S., 2004. Ultra-high resolution sediment analysis and diatom paleoecology from Effingham Inlet, British Columbia, Canada: Implications for late Holocene environmental change. Unpublished Carleton University Ph.D. Dissertation, 537 p.

Chang, A.S., Bertram, M.A., Ivanochko, I., Calvert, S.E., Dallimore, A., Thomson, R.E., 2013. Annual record of particle fluxes, geochemistry and diatoms in Effingham Inlet, British Columbia, Canada, and the impact of the 1999 La Niña event. Marine Geology. http://dx.doi.org/10.1016/j.margeo.2013.01.003.

Chang, A.S., Patterson, R.T., 2005. Climate shift at 4400 years BP: evidence from high-resolution diatom stratigraphy, Effingham Inlet, British Columbia, Canada. Palaeogeography, Palaeoclimatology, Palaeoecology 226, 72–92.

Chang, A.S., Patterson, R.T., McNeely, R., 2003. Seasonal sediment and diatom record from late Holocene laminated sediments, Effingham Inlet, British Columbia, Canada. Palaios 18, 477–494.

Chavez, F.P., Ryan, J., Lluch-Cota, S.E., Ñiquen, C.M., 2003. From anchovies to sardines and back: multidecadal change in the Pacific Ocean. Science 299, 217–221.

Christoforou, P., Hameed, S., 1997. Solar cycle and the Pacific 'centers of action'. Geophysical Research Letters 24, 293–296.

Crawford, W.R., Dewey, R.K., 1989. Turbulence and mixing: sources of nutrients on the Vancouver Island continental shelf. Atmosphere-Ocean 27, 428–442.

Dallimore, A., Thomson, R.E., Bertram, M.A., 2005. Modern to late Holocene deposition in an anoxic fjord on the west coast of Canada: implications for regional oceanography, climate and paleoseismic history. Marine Geology 219, 47–69.

Davis, J.C., 1986. Statistics and Data Analysis in Geology, second ed. Wiley, New York, 646 p.

Dean, W., Pride, C., Thunell, R., 2004. Geochemical cycles in sediments deposited on the slopes of the Guaymas and Carmen Basins of the Gulf of California over the last 180 years. Quaternary Science Reviews 23, 1817–1833.

Fleming, S.W., Clark, G.K.C., 2005. Attenuation of high-frequency interannual streamflow variability by watershed glacial cover. ASCE Journal of Hydraulic Engineering 131, 615–618.

Gergis, J.L., Fowler, A.M., 2009. A history of ENSO events since A.D. 1525: implications for future climate change. Climatic Change 92, 343–387.

Gershunov, A., Barnett, T.P., 1998. Interdecadal modulation of ENSO teleconnections. Bulletin of the American Meteorological Society 79, 2715–2725.

Goodrich, G.B., 2007. Influence of the Pacific decadal oscillation on winter precipitation and drought during years of neutral ENSO in the western United States. Weather and Forecasting 22, 116–124.

Gray, L.J., Beer, J., Geller, M., Haigh, J.D., Lockwood, M., Matthes, K., Cubasch, U., Fleitmann, D., Harrison, G., Hood, L., Luterbacher, J., Meehl, G.A., Shindell, D., van Geel, B., White, W., 2010. Solar influences on climate. Review of Geophysics 48, RG4001. http://dx.doi.org/10.1029/2009RG000282.

Grinsted, A., Moore, J.C., Jevrejeva, S., 2004. Application of the cross wavelet transform and wavelet coherency to geophysical time series. Nonlinear Process in Geophysics 11, 561–566.

Grossman, A., Morlet, J., 1984. Decompositions of Hardy functions into square integrable wavelets of constant shape. SIAM Journal on Mathematical Analysis 15, 732–736.

Haigh, R., Taylor, F.R., Sutherland, T.F., 1992. Phylotplankton ecology of Sechelt Inlet, a fjord system on the British columbiat coast. I. General festures of the nano- and microplankton. Marine Ecology Progress Series 89, 117–134.

Hameed, S., Lee, J.N., 2005. A mechanism for sun-climate connection. Geophysical Research Letters 32, L23817. http://dx.doi.org/10.1029/2005GL024393.

Hammer, Ø., Harper, D.A.T., Ryan, P.D., 2001. PAST, Paleontological statistics software package for education and data analysis. Palaeontologia Electronica 4 (9). http://www.palaeoelectronic.org/2001_1/past/issue1_01.htm.

Harris, S.L., Varela, D.E., Whitney, F.W., Harrison, P.J., 2009. Nutrient and phytoplankton dynamics off the west coast of Vancouver Island during the 1997/98 ENSO event. Deep-Sea Research II 56, 2487–2502.

Hartmann, B., Wendler, G., 2005. The significance of the 1976 Pacific climate shift in the climatology of Alaska. Journal of Climate 18, 4824–4839.

Hay, M.B., Pienitz, R., Thomson, R.E., 2003. Distribution of diatom surface sediment assemblages within Effingham Inlet, a temperate fjord on the west coast of Vancouver Island (Canada). Marine Micropaleontology 48, 291–320.

Hay, M.B., Calvert, S.E., Pienitz, R., Dallimore, A., Thomson, R.E., Baumgartner, T.R., 2009. Geochemical and diatom signatures of bottom water renewal events in Effingham Inlet, British Columbia (Canada). Marine Geology 262, 50–61.

Hemphill-Haley, E., Fourtanier, E., 1995. A diatom record spanning 114,000 years from Site 893, Santa Barbara Basin. In: Proceedings of the Ocean Drilling Program, Scientific Results, 146 (Part 2). Ocean Drilling Program, College Station, TX, pp. 223–249.

Hickey, B.M., 1998. Coastal oceanography of western North America from the tip of Baja California to Vancouver Island. In: Robinson, A.R., Brink, K.H. (Eds.), The Sea, pp. 345–391.

Hobson, L.A., McQuoid, M.R., 2001. Pelagic diatom assemblages are good indicators of mixed water intrusions into Saanich Inlet, a stratified fjord in Vancouver Island. Marine Geology 174, 125–138.

Hudgins, L., Friebe, C., Mayer, M., 1993. Wavelet transforms and atmospheric turbulence. Physical Review Letters 71, 3279–3282.

Hughen, K.A., Overpeck, J.T., Peterson, L.C., Anderson, R.F., 1996. The nature of varved sedimentation in the Cariaco Basin, Venezuela. In: Kemp, A.E.S. (Ed.), Palaeoclimatology and Palaeoceanography from Laminated Sediments. Geological Society Special Publication, vol. 116, pp. 171–183.

Ivanochko, T.S., Calvert, S.E., Thomson, R.E., Pedersen, T.F., 2008. Geochemical reconstruction of Pacific decadal variability from the eastern North Pacific during the Holocene. Canadian Journal of Earth Sciences 45, 1317–1329.

Labitzke, K., 2003. The global signal of the 11-year sunspot cycle in the atmosphere: when do we need the QBO? Meteorologische Zeitschrift 12, 209–216.

Lundholm, N., Hasle, G.R., 2010. *Fragilariopsis* (Bacillariophyceae) of the Northern Hemisphere – morphology, taxonomy, phylogeny and distribution, with a description of *F. pacifica* sp. nov. Phycologia 49, 438–460.

Mackas, D.L., Galbraith, M., 2002. Zooplankton community composition along the inner portion of Line P during the 1997–1998 El Niño event. Progress in Oceanography 54, 423–437.

Mackas, D.L., Peterson, W.T., Zamon, J.E., 2004. Compositions of interannual biomass anomalies of zooplankton communities along the continental margins of British Columbia and Oregon. Deep-Sea Research II 51, 875–896.

Mantua, N.J., Hare, S.R., 2002. The Pacific decadal oscillation. Journal of Oceanography 58, 35–44.

Mantua, N.J., Hare, S.R., Zhang, Y., Wallace, J.M., Francis, R.C., 1997. A Pacific interdecadal climate oscillation with impacts on salmon production. Bulletin of the American Meteorological Society 78, 1069–1079.

Maraun, D., Kurths, J., 2004. Cross wavelet analysis: significance testing and pitfalls. Nonlinear Process in Geophysics 11, 505–514.
McKay, J.L., Pedersen, T.F., Mucci, A., 2007. Sedimentary redox conditions in continental margin sediments (N.E. Pacific) — influence on the accumulation of redox-sensitive trace metals. Chemical Geology 238, 180–196.
McQuoid, M.R., Hobson, L.A., 1997. A 91-year record of seasonal and interannual variability of diatoms from laminated sediments in Saanich Inlet, British Columbia. Journal of Plankton Research 19, 173–194.
Meehl, G.A., Arblaster, J.M., Matthes, K., Sassi, F., van Loon, H., 2009. Amplifying the Pacific climate system response to a small 11-year solar cycle forcing. Science 325, 1114–1118.
Morlet, J., Arehs, G., Fourgeau, I., Girard, D., 1982. Wave propagation and sampling theory—Part I: Complex signal and scattering in multilayered media. Geophysics 47, 203–221.
Namias, J., 1978. Multiple causes of the North American abnormal winter 1976–77. Monthly Weather Review 106, 279–295.
Natural Resources Canada, 2009. The Atlas of Canada, mean total precipitation. http://atlas.nrcan.gc.ca/site/english/maps/environment/climate/precipitation/precip (last accessed March 2011).
Newman, M., Compo, F., Alexander, M., 2003. ENSO-forced variability of the Pacific decadal oscillation. Journal of Climate 16, 3853–3857.
Patterson, R.T., Fishbein, E., 1989. Re-examination of the statistical methods used to determine the number of point counts needed for micropaleontological quantitative research. Journal of Paleontology 63, 245–248.
Patterson, R.T., Fowler, A.D., 1996. Evidence of self–organization in planktic foraminiferal evolution: implications for interconnectedness of paleoecosystems. Geology 24, 215–218.
Patterson, R.T., Guilbault, J.-P., Thomson, R.E., 2000. Oxygen level control on foraminiferal distribution in Effingham Inlet, Vancouver Island, British Columbia, Canada. Journal of Foraminiferal Research 30, 321–335.
Patterson, R.T., Prokoph, A., Chang, A., 2004. Late Holocene sedimentary response to solar and cosmic ray activity influenced climate variability in the NE Pacific. Sedimentary Geology 172, 67–84.
Patterson, R.T., Prokoph, A., Kumar, A., Chang, A.S., Roe, H.M., 2005. Holocene variability in pelagic fish and phytoplankton productivity along the west coast of Vancouver Island, NE Pacific Ocean. Marine Micropaleontology 55, 183–204.
Patterson, R.T., Prokoph, A., Reinhardt, A., Roe, H.M., 2007. Climate cyclicity in late Holocene anoxic marine sediments from the Seymour-Belize Inlet Complex, British Columbia. Marine Geology 242, 123–140.
Patterson, R.T., Swindles, G.T., Roe, H.M., Kumar, A., Prokoph, A., 2011. Dinoflagellate cyst-based reconstructions of mid to late Holocene winter sea-surface temperature and productivity from an anoxic fjord in the NE Pacific Ocean. Quaternary International 235, 13–25.
Pickard, G.L., 1963. Oceanographic characteristics of inlets of Vancouver Island, British Columbia. Journal of the Fisheries Research Board of Canada 20, 1109–1144.
Prokoph, A., Barthelmes, F., 1996. Detection of nonstationarities in geological time series: wavelet transform of chaotic and cyclic sequences. Computers & Geoscience 22, 1097–1108.
Prokoph, A., Fowler, A.D., Patterson, R.T., 2000. Evidence for periodicity and nonlinearity in a high-resolution fossil record of long-term evolution. Geology 28, 867–870.
Prokoph, A., Patterson, R.T., 2004a. From depth scale to time scale: transforming of sediment image color data into high-resolution time series. In: Francus, P. (Ed.), Image Analysis, Sediment and Paleoenvironments. Developments in Paleoenvironmental Research Series, vol. 7, pp. 143–164.
Prokoph, A., Patterson, R.T., 2004b. Application of wavelet and discontinuity analysis to trace temperature changes: eastern Ontario as a case study. Atmospheres-Ocean 42, 201–212.
Prokoph, A., Adamowski, J., Adamowski, K., 2012. Influence of the 11-year solar cycle on annual streamflow maxima in southern Canada. Journal of Hydrology 442–443, 55–62.
Rogers, G.C., 1980. A documentation of soil failure during the British Columbia earthquake of 23 June, 1946. Canadian Geotechnical Journal 17, 122–127.
Sancetta, C., Calvert, S.E., 1988. The annual cycle of sedimentation in Saanich Inlet, British Columbia: Implications for the interpretation of diatom fossil assemblages. Deep-Sea Research 35, 71–90.
Sarno, D., Kooistra, W.H.C.F., Medlin, L.K., Percopo, I., Zingone, A., 2005. Diversity in the genus *Skeletonema* (Bacillariophyceae). II. An assessment of the taxonomy of *S. costatum*-like species with the description of four new species. Journal of Phycology 41, 151–176.
Schaaf, M., Thurow, J., 1994. A fast and easy method to derive highest-resolution time-series datasets from drillcores and rock samples. Sedimentary Geology 94, 1–10.
Schrader, H.J., Gersonde, G., 1978. Diatoms and silicoflagellates. Utrecht Micropaleontological Bulletin 17, 129–176.
Schulz, M., Stattegger, K., 1997. SPECTRUM, Spectral analysis of unevenly spaced paleoclimatic time series. Computers & Geosciences Journal 23, 929–945.
Schulz, M., Mudelsee, M., 2002. REDFIT, estimating red-noise spectra directly from unevenly spaced paleoclimatic time series. Computers & Geosciences Journal 28, 421–426.
Schwarzacher, W., 1993. Cyclostratigraphy and the Milankovitch Theory. Elsevier, Amsterdam, London.
Shabbar, A., Bonsal, B., Khandekar, M., 1997. Canadian precipitation patterns associated with the southern oscillation. Journal of Climate 10, 3016–3027.
Shen, C., Wang, W.-C., Gong, W., Hao, Z., 2006. A Pacific Decadal Oscillation record since 1470 AD reconstructed from proxy data of summer rainfall over eastern China. Geophysical Research Letters 33, L03702. http://dx.doi.org/10.1029/2005GL024804.
Sorgente, D., Frignani, M., Langone, L., Ravaioli, M., 1999. Chronology of Marine Sediments. Interpretation of activity-depth profiles of ^{210}Pb and other radioactive tracers: Part I. Technical Report No. 54. Consiglio Nazionale delle Ricerche. Instituto per la Geologia Marina, 32 p.
Stahl, K., Moore, R.D., McKendry, I.G., 2005. The role of synoptic-scale circulation in the linkage between large-scale ocean–atmosphere indices and winter surface climate in British Columbia, Canada. International Journal of Climatology 264, 541–560.
Stronach, J.A., Ng, M.K., Foreman, M.G., Murty, T.S., 1993. Tides and currents in Barkley Sound and Alberni Inlet. Marine Geodesy 16, 1–41.
Tabata, S., 1989. Trends and long-term variability of ocean properties at ocean station P in the northeast Pacific Ocean. In: Petersen, D.H. (Ed.), Aspects of Climate Variability in the Pacific and the Western Americas. Geophysical Monograph Series, vol. 55, pp. 113–132.
Thomson, R.E., 1981. Oceanography of the British Columbia coast. Canadian Special Publication of Fisheries and Aquatic Sciences 56, 291.
Thomson, R.E., Ware, D.M., 1996. A current velocity index of ocean variability. Journal of Geophysical Research 101, 14297–14310.
Thomson, R.E., Gower, J.F.R., 1998. A basin-scale oceanic instability event in the Gulf of Alaska. Journal of Geophysical Research 103, 3033–3040.
Thomson, R.E., Hickey, B.M., LeBlond, P.H., 1989. The Vancouver Island Coastal Current: fisheries barrier and conduit. In: Beamish, R.J., MacFarlane, G.A. (Eds.), Effects of Ocean Variability on Recruitment and an Evaluation of Parameters Used in Stock Assessment Models. Canadian Special Publications of Fisheries and Aquatic Sciences, vol. 108, pp. 265–296.
Torrence, C., Compo, G.P., 1998. A practical guide to wavelet analysis. Bulletin of the American Meteorological Society 79, 61–78.
Trenberth, K.E., Hurrell, J.W., 1994. Decadal atmosphere–ocean variations in the Pacific. Climate Dynamics 9, 303–319.
Trenberth, K.E., 1997. The definition of El Niño. Bulletin of the American Meteorological Society 78, 2771–2777.
Veizer, J., 2005. Celestial climate driver: a perspective from four billion years of the carbon cycle. Geoscience Canada 32, 13–30.
Ware, D.M., Thomson, R.E., 2000. Interannual to multidecadal timescale climate variations in the Northeast Pacific. Journal of Climate 13, 3209–3220.
Ware, D.M., Thomson, R.E., 2005. Bottom-up ecosystem trophic dynamics determine fish production in the Northeast Pacific. Science 308, 1280–1284.
Whitney, F.A., Welch, D.W., 2002. Impact of the 1997–1998 El Niño and 1999 La Niña on nutrient supply in the Gulf of Alaska. Progress in Oceanography 54, 405–421.
Zamon, J.E., Welch, D.W., 2005. Rapid shift in zooplankton community composition on the northeast Pacific shelf during the 1998-1999 El Niño – La Niña event. Canadian Journal of Fisheries and Aquatic Sciences 62, 133–144.
Zingone, A., Percopo, I., Sims, P.A., Sarno, D., 2005. Diversity in the genus *Skeletonema* (Bacillariophyceae). I. A reexamination of the type material of *S. costatum* with the description of *S. grevillei* sp. nov. Journal of Phycology 41, 140–150.